Remote Sensing of Environment xxx (xxxx) xxxx

Contents lists available at ScienceDirect

Remote Sensing of Environment

journal homepage: www.elsevier.com/locate/rse

Seamless retrievals of chlorophyll-*a* from Sentinel-2 (MSI) and Sentinel-3 (OLCI) in inland and coastal waters: A machine-learning approach

Nima Pahlevan[a,b,*], Brandon Smith[a,b], John Schalles[c], Caren Binding[d], Zhigang Cao[e], Ronghua Ma[e], Krista Alikas[f], Kersti Kangro[f], Daniela Gurlin[g], Nguyễn Hà[h], Bunkei Matsushita[i], Wesley Moses[j], Steven Greb[k], Moritz K. Lehmann[l], Michael Ondrusek[m], Natascha Oppelt[n], Richard Stumpf[o]

[a] NASA Goddard Space Flight Center, Greenbelt, MD, USA
[b] Science Systems and Applications, Inc. (SSAI), Lanham, MD, USA
[c] Creighton University, Department of Biology, Omaha, NE, USA
[d] Environment and Climate Change Canada, Burlington, ON, Canada
[e] Nanjing Institute of Geography and Limnology, Nanjing, China
[f] University of Tartu, Tartu, Estonia
[g] Wisconsin Department of Natural Resources, Madison, WI, USA
[h] VNU University of Science, Vietnam National University, Hanoi, Viet Nam
[i] University of Tsukuba, Ibaraki, Japan
[j] Naval Research Laboratory, Washington, D.C., USA
[k] University of Wisconsin-Madison, Space Science and Engineering, Madison, WI, USA
[l] Xerra Earth Observation Institute and the University of Waikato, Hamilton, New Zealand
[m] NOAA Center for Satellite Applications and Research, College Park, MD, USA
[n] University of Kiel, Department of Geography, Kiel, Germany
[o] NOAA National Center for Coastal Science Studies, Silver Spring, MD, USA

ARTICLE INFO

Edited by Menghua Wang

Keywords:
Chlorophyll-a
Sentinel missions
Water quality
Inland and coastal waters
Earth observation
Machine learning
Algorithm development

ABSTRACT

Consistent, cross-mission retrievals of near-surface concentration of chlorophyll-a (Chl*a*) in various aquatic ecosystems with broad ranges of trophic levels have long been a complex undertaking. Here, we introduce a machine-learning model, the Mixture Density Network (MDN), that largely outperforms existing algorithms when applied across different bio-optical regimes in inland and coastal waters. The model is trained and validated using a sizeable database of co-located Chl*a* measurements (n = 2943) and *in situ* hyperspectral radiometric data resampled to simulate the Multispectral Instrument (MSI) and the Ocean and Land Color Imager (OLCI) onboard Sentinel-2A/B and Sentinel-3A/B, respectively. Our performance evaluations of the model, via two-thirds of the *in situ* dataset with Chl*a* ranging from 0.2 to 1209 mg/m^3 and a mean Chl*a* of 21.7 mg/m^3, suggest significant improvements in Chl*a* retrievals. For both MSI and OLCI, the mean absolute logarithmic error (MAE) and logarithmic bias (Bias) across the entire range reduced by 40–60%, whereas the root mean squared logarithmic error (RMSLE) and the median absolute percentage error (MAPE) improved two-to-three times over those from the state-of-the-art algorithms. Using independent Chl*a* matchups (n < 800) for Sentinel-2A/B and -3A, we show that the MDN model provides most accurate products from recorded images processed via three different atmospheric correction processors, namely the SeaWiFS Data Analysis System (SeaDAS), POLYMER, and ACOLITE, though the model is found to be sensitive to uncertainties in remote-sensing reflectance products. This manuscript serves as a preliminary study on a machine-learning algorithm with potential utility in seamless construction of Chl*a* data records in inland and coastal waters, i.e., harmonized, comparable products via a single algorithm for MSI and OLCI data processing. The model performance is anticipated to enhance by improving the global representativeness of the training data as well as simultaneous retrievals of multiple optically active components of the water column.

* Corresponding author at: NASA Goddard Space Flight Center, Greenbelt, MD, USA.
E-mail address: nima.pahlevan@nasa.gov (N. Pahlevan).

https://doi.org/10.1016/j.rse.2019.111604
Received 15 August 2019; Received in revised form 4 December 2019; Accepted 9 December 2019

1. Introduction

As the primary pigment in phytoplankton, chlorophyll-*a* has historically been regarded as a proxy for biomass in the water column or living terrestrial plants. While an adequate amount of biomass is vital to a healthy and productive aquatic ecosystem, its excessive presence may be harmful, posing threats to public health (Brooks et al., 2016) and wildlife (Carmichael, 2001), and potentially detrimental to ecosystem function and health (Carvalho et al., 2013; Duan et al., 2009). Optical remote sensing has long been utilized as an effective observation methodology for providing estimates of near-surface concentration of chlorophyll-*a* (Chl*a*) in the open ocean (Smith and Baker, 1982; Yoder et al., 1993), as well as in coastal (Gordon et al., 1983) and inland waters (Bukata et al., 1981; Dekker et al., 1992; Jain and Miller, 1976; Mittenzwey et al., 1992; Yacobi et al., 1995). In principle, optical radiometric measurements of oceanic waters allow for accurate determination of ocean color, which is primarily governed by Chl*a* and any of its accessory pigments. In inland and coastal waters, the color is further modulated by the presence of organic and inorganic particles and dissolved matter (Mobley, 1994) rendering retrievals of Chl*a* a more challenging task.

Remotely sensed aquatic signals recorded at the top-of-atmosphere (TOA) are bulk optical properties emanating from the absorption (a) and scattering (b) of solar photons in the atmosphere, within the water column, and at the air-water interface. After accounting for the atmospheric effects, the TOA signal is reduced to the remote sensing reflectance (R_{rs}) – the ratio of water-leaving radiance to the total downwelling irradiance just above water – from which in-water optical properties are quantified. It is, therefore, the in-water absorption and scattering, or in a more general sense, the Inherent Optical Properties (IOPs), that determine the color of water. Recognizing this physical principle, widely used Chl*a* retrieval algorithms can take two forms, namely semi-analytical approaches, which derive IOPs from R_{rs} and then estimate Chl*a*, and semi-empirical methods that estimate Chl*a* directly from R_{rs}. The former approach commonly relies on estimates of phytoplankton specific absorption (a_{ph}^*) peaks within the red portions of the spectrum, e.g., $a_{ph}^*(670)$ (Gons, 1999; Lee et al., 2002; Odermatt et al., 2018; Schroeder et al., 2007) and has proven to perform satisfactorily in some aquatic ecosystems (Odermatt et al., 2018).

Using the underlying physics driven by phytoplankton absorption and backscattering properties, semi-empirical methods typically employ band combinations of R_{rs} in the blue-green (O'Reilly et al., 1998) or in the red and near-infrared (NIR) regions (Gitelson, 1992). This category also comprises line-height (LH) approaches that utilize a combination of three bands in either red or red-NIR band(s) to compute characteristic peaks in the spectral reflectance associated with Chl*a*. Examples of this scheme include the Maximum Chlorophyll Index (MCI) (Gower et al., 2005), the Fluorescence Line Height (FLH) (Letelier and Abbott, 1996), or the Maximum Peak Height (MPH) (Matthews et al., 2012). The blue-green ratio assumes that the magnitude and the shape of the reflectance spectrum are primarily governed by Chl*a* with minimal effects from organic/inorganic material within the upper water column. More than two decades of research have revealed certain advantages and disadvantages associated with the blue-green ratio method. Many studies have shown that while the blue-green ratio correlates well with Chl*a*, performs well in clear waters, and provides a good indication of the relative distribution of biomass, it often tends to overestimate Chl*a* in inland and coastal waters (Freitas and Dierssen, 2019; Le et al., 2013; McKee et al., 2007; Novoa et al., 2012; Tang et al., 2003; Tzortziou et al., 2007). The polynomial coefficients of the blue-green ratio algorithm (hereafter referred to as OC) have recently been fine-tuned based on spectral configurations of various satellite sensors, including the Sea-viewing Wide Field-of-View Sensor (SeaWiFS), the MODerate resolution Imaging Spectroradiometer (MODIS), the Operational Land Imager (OLI), and the MEdium Resolution Imaging Spectrometer (MERIS) (O'Reilly and Werdell, 2019).

On the other hand, the red-NIR method assumes a negligible absorption by colored dissolved organic matter (a_{CDOM}) and non-algal particles (a_{NAP}) as well as spectrally invariant backscattering in the red and NIR region (Gitelson, 1992; Gitelson et al., 2007; Gower and Borstad, 1990). This approach has shown promise for biomass retrievals in phytoplankton-dominated mesotrophic, eutrophic, or hypereutrophic waters and is not intended for use in waters with low Chl*a*, where the reflectance in red and NIR regions are not sensitive to variations in Chl*a* (Gitelson et al., 2009; Gurlin et al., 2011; Moses et al., 2009a). Various formulations of this approach have been adopted for MERIS spectral bands to retrieve Chl*a* (Gilerson et al., 2010; Gower and King, 2012). Recently, based on a previously developed hybrid methodology for open-ocean retrievals (Hu et al., 2012), Smith et al. (2018) proposed a weighting scheme (hereafter referred to as Blend) combining the two band-ratio algorithms: the OCx (Hu et al., 2012; O'Reilly et al., 1998; O'Reilly and Werdell, 2019) and a red-NIR 2-Band ratio (see Appendix A for Eqs. (A.6) and (A.8)) (Moses et al., 2012). These methods based upon red or NIR bands, including LH and band ratios, are thought to be less sensitive to uncertainties in atmospheric correction. Essentially, one could perform Chl*a* retrievals using Rayleigh-corrected spectral reflectance and/or radiance (Matthews et al., 2012; Matthews and Odermatt, 2015; Wynne et al., 2010).

Other mathematical methods (Giardino et al., 2007) have also been proposed; however, their utilities have not been widely evaluated. Statistical approaches like neural networks (NN) have also been shown to perform reasonably well through a few different studies. Vilas et al. (2011) implemented a Multilayer Perceptron NN trained for three different water types and reported MERIS-derived Chl*a* retrievals with RMSEs ~0.8 mg/m^3 with a mean of ~2.5 mg/m^3 and a range of 0.03–8 mg/m^3 in coastal waters of Galician *rias* (northwest coast of Spain). They asserted that their strategy led to improved performances compared to the standard NN approach implemented in the MERIS data processing scheme (Doerffer and Schiller, 2007; Schroeder et al., 2007). Also, Binding et al. (2011) and Palmer et al. (2015) showed that, for MERIS data processing, the LH approaches perform better than NN-based Chl*a* retrievals in eutrophic waters of Lake of the Woods and Lake Balaton with Chl*a* >10 mg/m^3; however, one of the NN processors (Schroeder et al., 2007) was shown to outperform the rest within the lower ranges of Chl*a*. Given various degrees in the sensitivity of Chl*a* algorithms to different water types, water-type retrieval algorithms have drawn major attention (Moore et al., 2001; Neil et al., 2019; Spyrakos et al., 2018; Vertucci and Likens, 1989). These methods, however, require more extensive development/validation data and are highly impacted by uncertainties in the atmospheric correction rendering reliable water-type classification a daunting task (Neil et al., 2019).

One major disadvantage in most of these research activities is the limited availability of extensive *in situ* radiometric and biogeochemical data (Palmer et al., 2015). The availability of such data may furnish a more representative dataset enabling enhancements in Chl*a* retrieval algorithms and their validations (Mouw et al., 2015). Recent launches of Sentinel-2 and Sentinel-3 with sensors capable of quantifying in-water optical properties have spurred the science community to strive to devise improved methods for retrievals of Chl*a* and other water constituents (Ansper and Alikas, 2019; Cazzaniga et al., 2019; Gernez et al., 2017; Toming et al., 2016). This manuscript introduces a robust machine-learning approach for seamless estimations of Chl*a* in inland and nearshore coastal waters from the MultiSpectral Instrument (MSI) and the Ocean and Land Color Imager (OLCI) aboard the Sentinel-2 and Sentinel-3 missions, respectively. That is, we aim to produce consistent, analogous cross-mission Chl*a* products through a single algorithm. The developed algorithm, a class of neural networks known as a Mixture Density Network (MDN), is trained with 1000 co-located *in situ* R_{rs} – Chl*a* pairs. We demonstrate the performance of the model against a number of alternate, previously published algorithms (e.g., OC and Blend) using two-thirds of the entire *in situ* data (n ~ 1943; Fig. 1)

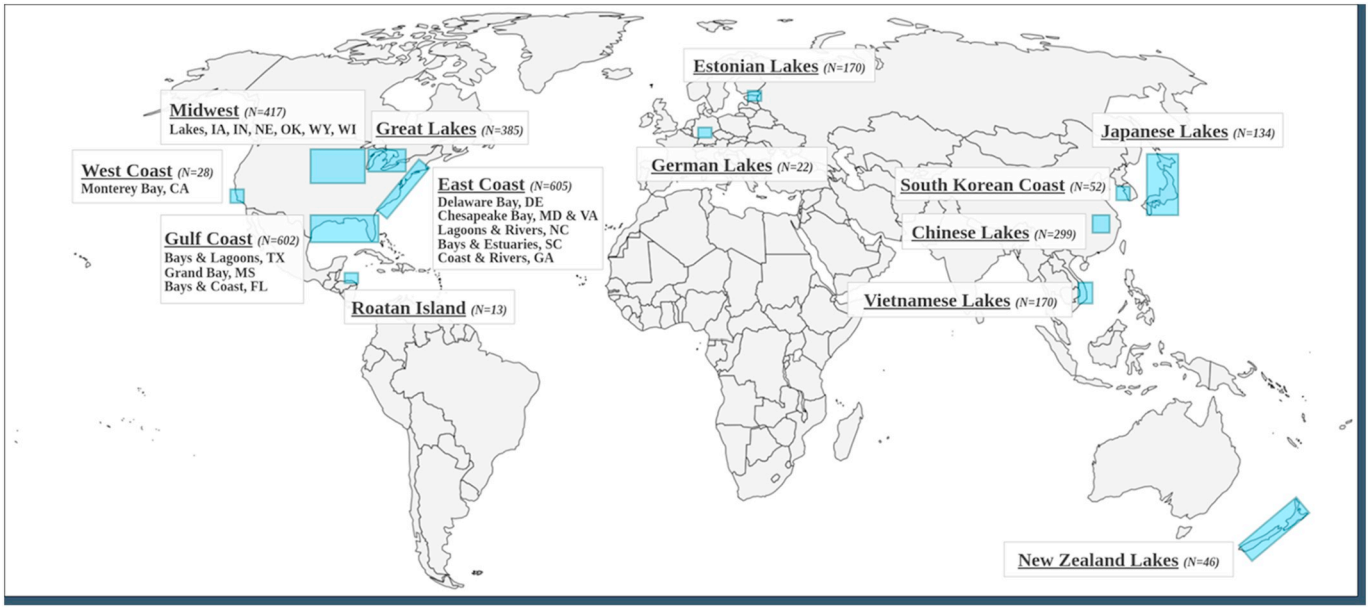

Fig. 1. Spatial distribution of the sites where development data, i.e., water quality data and radiometric measurements, were acquired. Our database encompasses a fairly extensive set of bio-optical and bio-geochemical conditions in rivers, bays, lakes, reservoirs, lagoons, and coastal estuaries.

acquired in many different typically optically deep waters, i.e., effects of bottom reflection are assumed negligible. This manuscript follows with a description of the *in situ* dataset, the MDN model, its various components, and its performance assessment. The model performance is further assessed using independent *in situ* Chl*a* matchups coinciding with MSI and OLCI overpasses, whereby its sensitivity to uncertainties in R_{rs} is inferred for practical applications. This is followed by a discussion of the implications for cross-mission consistency for reliable monitoring of inland and nearshore coastal waters.

2. Development data

For this study, *in situ* radiometric and biogeochemical data originating from several regions whose optical regimes span a broad range of trophic states were compiled. The geographic distribution of the sites is provided in Fig. 1. These aquatic ecosystems, including rivers, bays, lakes, reservoirs, lagoons, and coastal estuaries, are influenced by various human-induced activities (e.g. application of fertilizers for agricultural purposes in watersheds of Wisconsin lakes) and climate-change-related pressure (e.g., flash floods in Vietnam). Some of the lakes (e.g., Lake Taihu; (Duan et al., 2009)) are well-known for their long history of harmful algal blooms (HABs), whereas some others are relatively deep, clear waters (e.g., Lake Taupo, New Zealand). The diversity in their biogeochemical characteristics (see distributions in Fig. 2), representing various land-use and utilities, provides an unprecedented opportunity for algorithm developments and validations, likely establishing a pathway towards generating improved global Chl*a* products. Typical biogeochemical properties for a handful of sites identified based on their regions or countries are summarized in Table 1.

2.1. Radiometry

The radiometric quantity used in this research is R_{rs} computed as

$$R_{rs} = L_w(0^+)/E_d(0^+) \quad (1)$$

where L_w and E_d are the water-leaving radiance and total downwelling irradiance evaluated just above the water, respectively. The wavelength-dependency has been dropped for brevity. Overall, four different measurement methods were followed for *in situ* measurements of R_{rs}. A portion of data was obtained using sequential measurements of the water surface, sky, and plaque radiances by a single handheld radiometer (ASD FieldSpec®) following the ocean optics protocol (Matsushita et al., 2015; Mueller et al., 2003). Some measurements were made via a pair of intercalibrated (Ocean Optics® or RMSES®) spectrometers with one measuring subsurface upwelling radiance and the other measuring total downwelling irradiance above the surface (e.g., Nebraska Lakes and Reservoirs) (Gitelson et al., 2009). In deeper coastal waters (e.g., Chesapeake Bay), the free-fall profiling technique (Mueller et al., 2003) was adopted. Further, a fraction of data (e.g., New Zealand lakes) was collected using the sky-block approach which allows direct measurements of $L_w(0^+)$ using a cone to avoid unwanted surface-reflected radiances (Lee et al., 2013). HyperOCR® radiometers were used to collect data with the free-fall profiling and sky-block techniques. A data-quality screening was carried out to exclude outliers identified through visual inspections of R_{rs} data exhibiting abnormal spectral features, highly inconsistent with known spectral properties of constituents measured in the water. The discarded data amounted to only a small fraction (< 1%) of the initial database, which was not surprising because the data had undergone preliminary quality screening by the data providers. The radiometric data were provided at various spectral resolutions (between 1 and 3.3 nm) mostly within the 350–900 nm range. The hyperspectral data were then convolved with the relative spectral responses of MSI (Drusch et al., 2012; Pahlevan et al., 2017b) and OLCI (Donlon et al., 2012) to simulate band-equivalent R_{rs} for algorithm training and testing.

2.2. Chlorophyll-a

As indicated in Table 1, our dataset represents a wide array of biogeochemical properties originating from various geographic regions (Fig. 1). At each station a set of water quality parameters was measured from surface water samples collected at a depth of 0.5 m below the surface and stored refrigerated in the dark. These surface samples were filtered on the day of collection on filter pads (e.g., Gelman A/E and Whatman GF/F) and frozen for laboratory analyses.

Chlorophyll-a was then extracted from the water samples using 100% methanol, 96–99.5–100% ethanol (Jeffrey and Humphrey, 1975), or 90–99.5% acetone, and then its concentration was measured fluorometrically (Welschmeyer, 1994) or spectrophotometrically

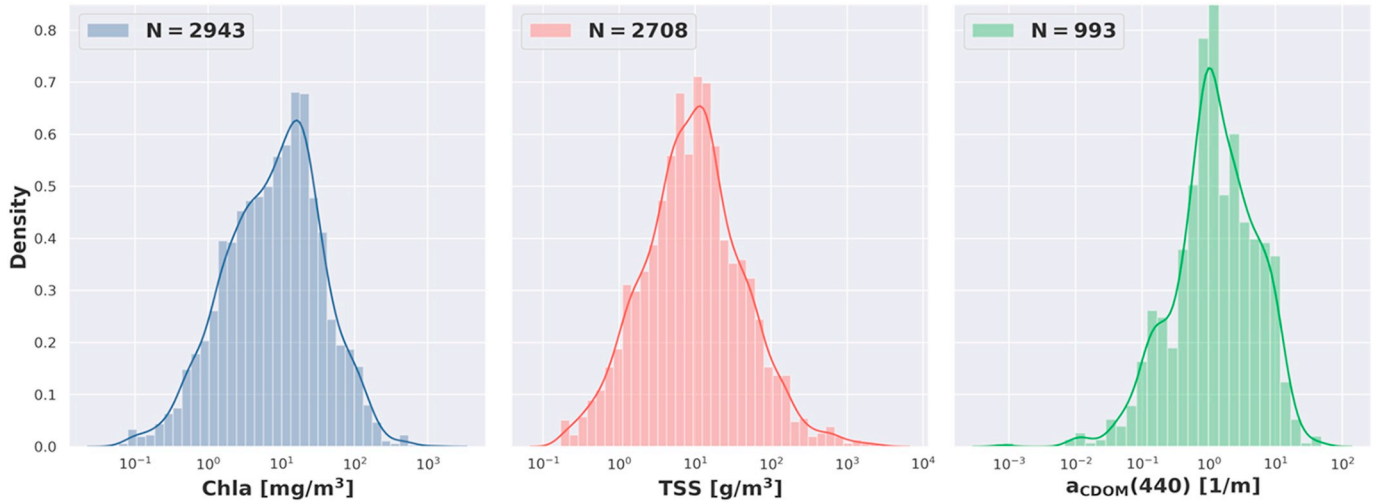

Fig. 2. Log distribution of all available Chl*a*, TSS, and $a_{CDOM}(440)$ included in our database. The median and mean values for this triplet of water quality parameters are (8.9, 21.7) mg/m^3, (9.6, 34.7) g/m^3, and (1.2, 2.8) 1/m, respectively.

(Buschmann et al., 2000; Holm-Hansen and Riemann, 1978). Since some of the Chl*a* measurements were not corrected for pheophytin and/or other pigments' contribution, using ~1316 corrected-uncorrected pairs available through the Great Lakes dataset, we identified a fourth-order polynomial ($R^2 = 0.96$) that best fit the data. This is regarded as a first-order correction applied to the uncorrected Chl*a* to diminish impacts of pheophytin and/or other pigments.

In addition to Chl*a*, other water quality indicators, such as near-surface concentration of total suspended solids (TSS), and a_{CDOM}, Secchi disk depth, and turbidity were also measured. Fig. 2 illustrates the frequency distribution of co-located TSS and a_{CDOM} measurements along with Chl*a*. The Chl*a* histogram follows a log-normal distribution, with a mean and standard deviation of 21.7 and 47.5 mg/m^3, respectively, indicating a wide range of water conditions, including oligotrophic lakes (Chl*a* < 4 mg/m^3), moderately eutrophic coastal waters, and hypereutrophic lakes (Chl*a* ~1209 mg/m^3). Note, however, that only 5% of data (~150) is representative of hypereutrophic waters (90 < Chl*a* < 1209 mg/m^3). The variability in co-located a_{CDOM} and TSS measurements further affirms the semi-global representativeness of this dataset, comprising ecosystems with moderately clear, moderately eutrophic waters, and organic−/sediment-rich waters. Of the entire set of R_{rs} – Chl*a* pairs, about 90% were accompanied by TSS measurements and approximately one-third came with a_{CDOM} measurements (Fig. 2).

3. Methodology

3.1. Model development

In remote sensing of water quality, retrieving a water quality parameter like Chl*a* from an R_{rs} spectrum is often an ill-posed problem, i.e., multiple Chl*a* values may correspond to a single R_{rs} spectrum (Defoin-Platel and Chami, 2007; Sydor et al., 2004; Yang et al., 2011). This is because Chl*a* is only one of several optically active components contributing to the R_{rs} spectrum, whose spectral features might overlap with those of Chl*a* (e.g., Chl*a* absorption in the blue region overlaps with that of CDOM). As a result, various combinations of constituent concentrations and bio-optical conditions can correspond to a single R_{rs} spectrum, giving rise to the problem of non-uniqueness of the solution. The Mixture Density Network (MDN) utilized here is able to overcome this non-uniqueness problem to a great extent.

3.1.1. Mixture density networks

MDNs are a class of neural networks whose outputs parameterize a mixture of Gaussians (Bishop, 1994). In understanding MDNs, it is

Table 1
Median and standard deviation (Std) of biogeochemical properties, i.e., Chl*a*, a_{CDOM}, and near-surface concentration of total suspended solids (TSS), for *select* sites. Seasons refer to northern meteorological seasons.

Region (years) (samples)	Lake/bay/estuary	Season	Chl*a* (mg/m^3)		$a_{CDOM}(440)$ (1/m)		TSS (g/m^3)		Reference
			Median	Std	Median	Std	Median	Std	
Midwest U.S. Lakes	Nebraska (NE) lakes and reservoirs	Spring	10.2	37.1	0.72	0.23	3.56	3.50	(Gurlin et al., 2011)
(2008–2016)		Summer	27.5	46.1	0.74	0.21	8.00	10.1	
(N = 392)		Fall	40.8	43.8	0.72	0.24	8.67	9.80	
	Wisconsin (WI) lakes and flowages	Spring	3.90	4.2	0.49	0.26	4.25	3.18	Unpublished
		Summer	8.79	120	0.70	2.43	4.40	16.1	
		Fall	25.1	29.4	1.15	1.63	6.10	8.47	
Estonia	Lake Peipsi, Lake Võrtsjärv, small lakes	Spring	15.14	10.9	3.27	9.29	4.67	4.43	(Ansper and Alikas, 2019)
(2015–2018)		Summer	13.18	14.4	2.14	4.70	7.64	5.74	
(N = 193)		Fall	20.53	17.3	1.66	1.69	8.25	5.62	
Germany	Lake Kummerow	Spring	8.9	3.7	1.32	1.13	–	–	(Dörnhöfer et al., 2018)
(2015–2017)		Summer	14.4	5.6	1.28	0.12	1.7	2.7	
(N = 22)		Fall	12.3	5.5	0.94	0.03	3.0	1.5	
U.S. East Coast	Chesapeake and Delaware Bays	Summer	29.4	86.9	0.62	0.07	10.7	27.4	(Gitelson et al., 2007; Schalles, 2006)
(2002–2015)	Carolina	Summer	15.8	14.3	3.8	5.5	36.8	26.5	
(N = 767)	Georgia	Summer	12.8	12.3	1.04	3.0	21.5	25.3	
	Florida coasts	Summer	41.9	30.3	1.14	0.22	14.9	7.9	

helpful to first clarify the problem they seek to solve. Standard machine learning approaches can be regarded as function approximators; they attempt to find a function $f(x) = y$ such that an error metric (e.g., the root mean squared error; RMSE), gauged against some dataset $D \subset R$, is minimized. This desired function has a restriction (Schmidt, 2011):

$$\forall\ (x,y) \in D \wedge (x,y') \in D \Rightarrow y = y' \tag{2}$$

That is, the function must be right-unique within the dataset, guaranteeing there is at most a single value of y for any x. The problem with this requirement arises when we wish to find the inverse function, $x = f^{-1}(y)$. In this situation, we can no longer guarantee a unique mapping: if there were many x values mapped to the same y value, the situation will now be reversed, i.e., multiple values of x being mapped to a single value of y.

Instead of directly estimating the target variable, MDN produces three statistical measures of the variable, namely, a mean vector (μ), a covariance matrix (Σ), and a mixing coefficient (α) for each Gaussian modeled. MDNs are designed to solve the issue of a many-to-one inverse problems by modeling a conditional probability distribution over the range of the target variable(s) (Sydor et al., 2004; Yang et al., 2011). Recall that the goal of a machine learning model is to fit a function of the form:

$$f: X \subset R^n \rightarrow Y \subset R^m$$

With c as the number of Gaussians modeled, the number of outputs of the network is then equal to $c * \left(1 + m + \frac{m*(m+1)}{2}\right)$: a single mixing coefficient, m means, and $\frac{m*(m+1)}{2}$ outputs, which define the lower triangle of covariance matrix. The learned probability density is then defined as:

$$p(y \mid x) = \sum_{i=1}^{c} \alpha_i(x)\, \phi_i(y \mid x) \tag{3}$$

where ϕ_i is a normal distribution with μ, Σ as the mean vector and the covariance matrix. A valid Gaussian mixture of this form, however, requires that the output variables adhere to the following constraints: the mixing coefficients, α_i, must add to 1; and the covariance matrix Σ must be positive, definite, and regularized for small ϵ. The Gaussians are combined to form the final output estimation via maximum likelihood, which represents the estimate in the area of highest probability mass:

$$\hat{y} = \mu_i(x): i = argmax\ \alpha(x) \tag{4}$$

3.1.2. Input and output

A total of 1000 randomly chosen pairs of R_{rs} – Chl*a* were supplied for training the model, leaving out the rest of the data for testing. Following several experiments on the size of the training subset, we found that increasing the proportion of training data versus the testing data introduces insignificant changes in the model performance; hence, approximately only one-third (n = 1000) of the development data was used for training, leaving out adequate test samples for categorical assessments of the performances (e.g., Table 3). Input to the model consists solely of MSI- and OLCI-simulated R_{rs} within the 400–800 nm range. This data includes seven MSI and 12 OLCI bands. OLCI's 400-nm band is excluded due to inadequate numbers of radiometric spectra with measurements <400 nm. This strategy prevents a major reduction in the size of the training/validation dataset. Also, OLCI's three oxygen bands in the proximity of 760-nm were not considered due to other applications foreseen for these bands (Mei et al., 2017; Preusker and Lindstrot, 2009). All features are log-transformed, normalized based on median centering and interquartile scaling, and then scaled to the range (0,1); output variables are subject to the same normalization method. This procedure is robust to outliers which may be present in the data, while also enforcing a homogeneous scale and distribution across features. The final range scaling ensures all feature information is contained within the valid domain for the rectified linear unit (ReLU) activation functions (Agarap, 2018). The output of the model in this paper consists of the single variable, Chl*a*; thus, reducing covariance matrices (Σ) to standard deviations (σ). This is a practical necessity rather than a theoretical one. That is, modeling multiple output variables should improve overall estimates, but would require co-located measurements of all variables, such as Chl*a*, TSS, and IOPs, for all training samples. In spite of using solely Chl*a* as the output, however, an MDN still learns to distinguish different distributions conditioned upon the input R_{rs}, which leads to improvement over standard models. Fig. 3 illustrates a schematic block diagram of our developed MDN model.

3.1.3. Hyperparameters

There are a number of hyperparameters to tune, including the number of Gaussian distributions which are modeled, as well as all standard neural network hyperparameters (e.g. regularization and learning rates, network size and depth, etc.). These choices appear to be fairly robust to changes within the current implementation, especially with regard to the MDN-specific parameters. Following experimenting with several architectures, we found that the model is very robust to changes in various hyperparameters. The Chl*a* performance retrievals, for instance, varied only <1% for the following scenarios: a) a two-layer network with 20 neurons in each and 2 mixture functions versus b) a 10-layer network each having 200 neurons with 10 mixture functions. For practical matters, therefore, we chose to use a five-layer neural network with 100 neurons per layer, which is trained to output the parameters of five Gaussians. From this model, the overall estimate is selected via the Gaussian with the maximum likelihood. The median estimates from the MDN model taken over ten trials of random network initializations are the predicted Chl*a* for a given R_{rs} spectrum. Here, the same training data are used for all trials.

3.2. Comparison with state-of-the-art algorithms

To evaluate the performance of MDN using simulated MSI and OLCI *in situ* radiometric data, the precision and accuracy in Chl*a* retrievals is compared with those from select state-of-the-art algorithms (Hu et al., 2012; Mishra and Mishra, 2012; Moses et al., 2009b; Moses et al., 2012; O'Reilly et al., 1998; O'Reilly and Werdell, 2019; Smith et al., 2018). The algorithms examined are relevant OC algorithms, 2-Band, 3-Band, and the Normalized Difference Chl*a* Index (NDCI) (see Appendix A). Our preliminary analyses indicated that OC, i.e., OC3 and OC4, and Blend outperform other existing algorithms and allow for retrievals over a comparable range of Chl*a*. Hence, for conciseness, we primarily focus on these two algorithms as benchmarks. In addition to the global statistical analysis, to gain insights into the utility of MDN in various eutrophic conditions, a stratified analysis defined according to the trophic state indices (TSI) (Carlson, 1977) was carried out. For the implementation of various algorithms, *in situ* $R_{rs}(\lambda)$ are resampled with the relative spectral response functions of MSI and OLCI and then supplied to the target algorithms. The exception was the OC algorithms for which $R_{rs}(\lambda)$ are resampled with 11-nm square bands positioned at the band centers to ensure consistency with the original developments of the algorithms, i.e., the fourth-order polynomial coefficients are derived for 11-nm square spectral bands (O'Reilly et al., 1998; O'Reilly and Werdell, 2019).

3.3. Atmospheric correction

The impacts of atmospheric correction (AC) on MDN and select existing algorithms are tested to better understand how uncertainties in AC propagate to Chl*a* products. In doing so, three AC methods, namely the SeaWiFS Data Analysis System (SeaDAS), POLYMER, and ACOLITE, whose utility for processing MSI and OLCI have been demonstrated (Mograne et al., 2019; Pahlevan et al., 2019; Warren et al., 2019), are utilized. For this exercise, we investigate image data from both MSI-A

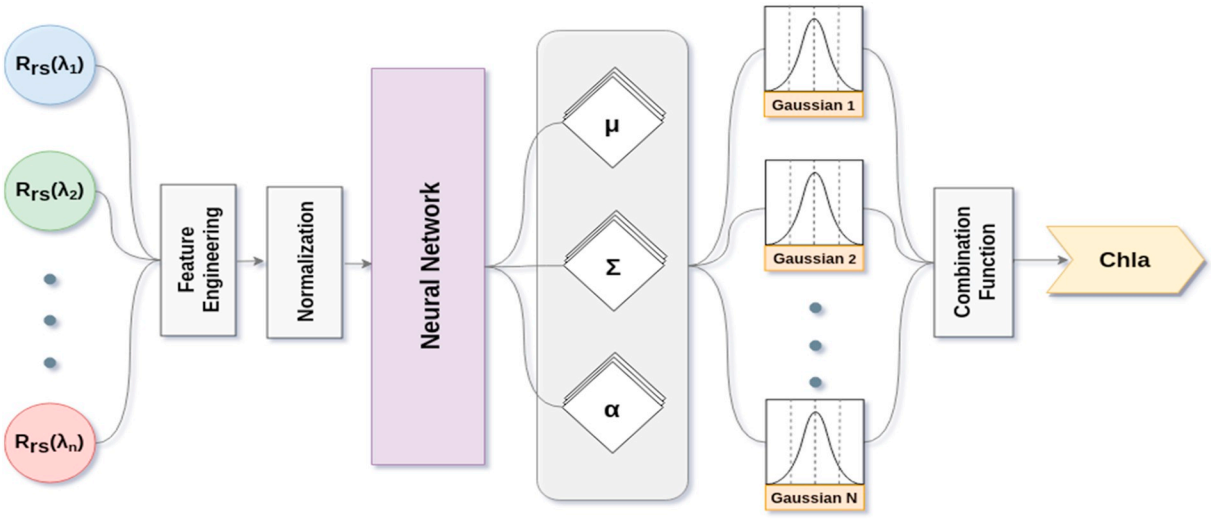

Fig. 3. Schematic block diagram illustrating the main components of a Mixture Density Network (MDN), a class of neural networks that estimates multivariate probability density functions with their corresponding parameters ($\boldsymbol{\mu}$, Σ) and mixing coefficients ($\boldsymbol{\alpha}$) to arrive at an optimal Chla retrieval. Note that a covariance matrix (Σ) is reduced down to standard deviation (σ) when a single target variable (e.g., Chl*a*) is sought.

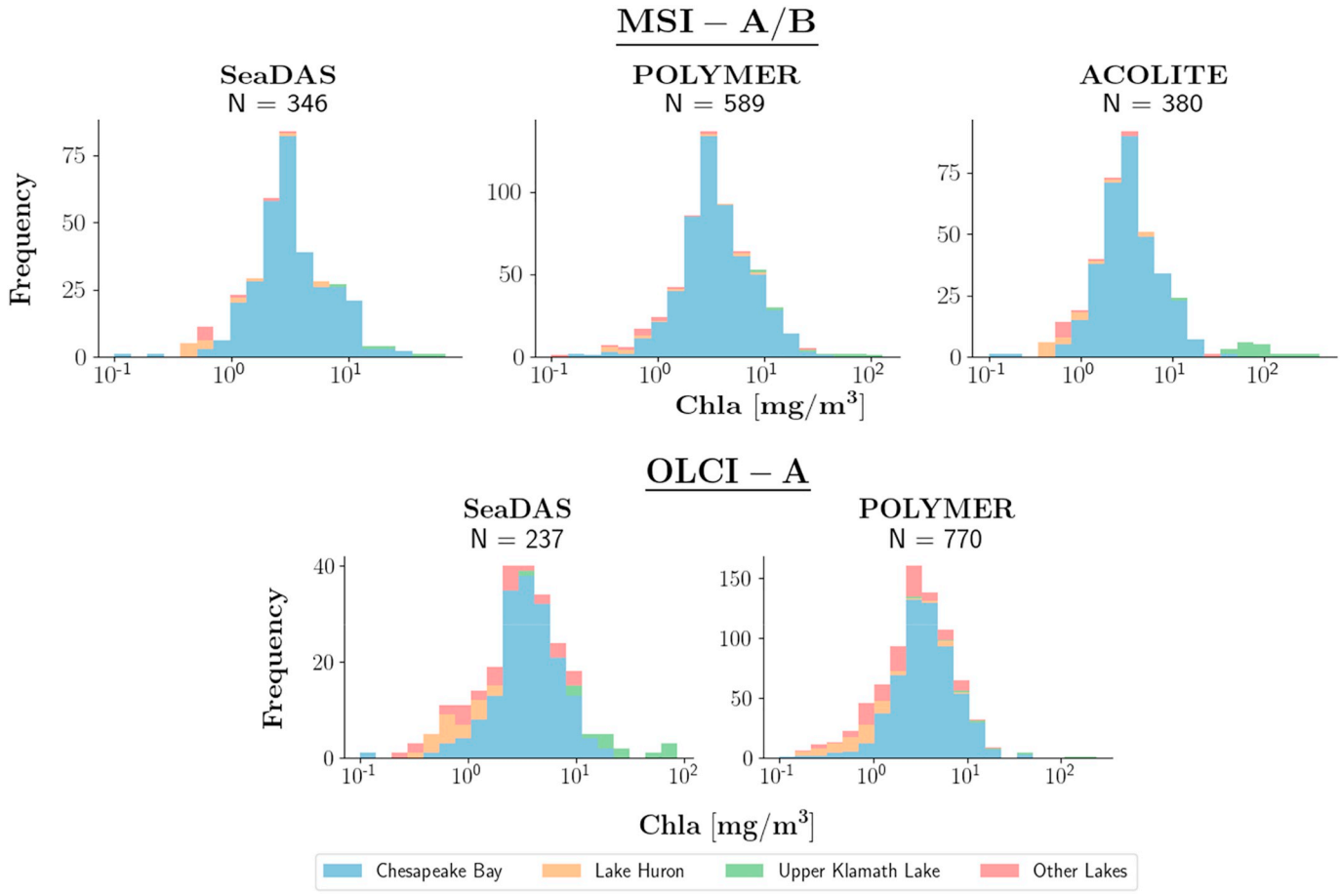

Fig. 4. Stacked bar charts demonstrating the distribution of valid *in situ* Chl*a* matchups identified under MSI-A/B and OLCI-A overpasses in a few select sites across North America. The data mostly come from the Chesapeake Bay due to a continuous data collection scheme. The AC processors have different exclusion criteria resulting in different number of valid matchups. The Other Lakes refer to the Great Lakes (other than Lake Huron) and Simcoe Lake. For MSI, >85% data are from the Chesapeake Bay autonomous buoy data.

and MSI-B; nevertheless, only OLCI-A data are evaluated due to inadequate matchups for OLCI-B. For brevity, we continue to refer to them as MSI and OLCI, unless otherwise noted.

SeaDAS estimates aerosol loading and their optical properties using a band ratio of Rayleigh-corrected reflectance computed using two NIR bands or one NIR and one shortwave infrared (SWIR) band (NIR-SWIR) (Gordon and Wang, 1994). The estimated aerosol contribution in the NIR and/or in the NIR-SWIR bands are then extrapolated to the visible

bands and subtracted from the Rayleigh-corrected signal. In this study, the band combinations of 865–1613 nm for MSI (Pahlevan et al., 2017b) and 779–865 nm for OLCI are applied for the removal of aerosol contribution (SeaDAS v7.5). Note that for the MSI processing, a 5 × 5 median filter was applied to Rayleigh-corrected radiances prior to R_{rs} retrievals (Pahlevan et al., 2017b), whereas *no* spatial smoothing filter was applied to OLCI data, assuming an adequate radiometric performance at its 300-m ground sample distance (Donlon et al., 2012). The vicarious calibration gains for both MSI (Pahlevan et al., 2019) and OLCI (ESA and EUMETSAT, 2019) were implemented, however. We also excluded pixels that did not pass through the standard Level-2 flags, i.e., land, high/saturated radiance, stray light, and cloud/ice.

POLYMER (Steinmetz et al., 2011) is a spectral matching algorithm that finds the best fit to an observed TOA reflectance among a collection of modeled signals with contributions from aerosol and molecular scattering, any glitter signal (e.g., surface glint or enhanced signal arising from haze), and R_{rs}. Three polynomial coefficients are used to describe the aerosol scattering and glitter and two are used to vary R_{rs} as a function of Chl*a* and particulate backscattering coefficient. POLYMER has been shown (Frouin et al., 2012) to work well in areas impacted by glint and/or where adjacency effects may be present (Bulgarelli et al., 2014; Santer and Schmechtig, 2000). Using an extensive radiometric dataset collected in the Baltic Sea and the Western English Channel, as well as a few lakes, Warren et al. (2019) has recently identified POLYMER as an optimal atmospheric correction method for optically complex waters. Here, we will utilize POLYMER (v4.11), which includes all the default exclusion criteria but does *not* incorporate any vicarious calibration gains. The output radiometric products were scaled by π for consistency in units (1/sr).

ACOLITE, whose performance for Landsat-8 imagery has shown promise in highly turbid waters (Vanhellemont and Ruddick, 2014), was also applied to MSI images only. The current version of ACOLITE (20190326.0), nevertheless, applies a dark spectrum fitting (DSF) scheme as the default setting (Vanhellemont, 2019), which was used in this experiment. The DSF assumes a) a homogeneous atmosphere over a certain extent of an image and b) that there are pixels within this subscene that contain near-zero water-leaving radiances in one band. Similar to the scheme implemented in SeaDAS or land-based atmospheric correction methods (Vermote et al., 2016), a pre-generated look-up-table is utilized to find dominant aerosol conditions. The corresponding R_{rs} products were output and passed to the Chl*a* retrieval algorithms.

MSI- and OLCI-derived R_{rs} produced via these processors are then supplied to MDN, OC, and Blend to generate Chl*a* products. The products are evaluated using *in situ* Chl*a* matchups identified under Sentinel-2A/B and Sentinel-3A overpasses in the Chesapeake Bay, the Upper Klamath Lake (OR), the Great Lakes, as well as Lake Winnipeg and Lake Simcoe in Canada. These data (Fig. 4) are acquired through routine state and/or federal monitoring activities through either field visits and laboratory analyses, i.e., lake data; https://www.canada.ca/en/environment-climate-change/services/freshwater-quality-monitoring/online-data.html, or autonomous, on-site fluorometric measurements available via multiple buoys in the Chesapeake Bay maintained and operated by the National Oceanic and Atmospheric Administration (NOAA), i.e., https://buoybay.noaa.gov. The lake data are mostly provided by the Environment and Climate Change Canada (ECCC) and the Upper Klamath Lake data were obtained from the Water Quality Portal (WQP; https://www.waterqualitydata.us). The reasoning behind the choice of these datasets was their easy access and coverage of a wide range of trophic conditions. We used near-surface measurements in all sites except those made in the Great Lakes, where depth-integrated Chl*a* values were made available by ECCC. Further, using the method briefly described in Section 2.2, the available fluorometric data were partially corrected for other pigments. Valid matchups were selected according to certain spatial and temporal constraints. The spatial analysis was carried out within 3 × 3 – element windows centered around the matchup location. The matchup was considered valid if ≥5 pixels are labeled with valid Chl*a* values; hence, nearshore matchups are discarded. The median value is computed to represent image-derived Chl*a* (Werdell and Bailey, 2005). For the Chesapeake matchups, data available within ±30 min of satellite overpasses were utilized, whereas a wider time span (±3 h) was adopted for lake matchups (Werdell and Bailey, 2005). Fig. 4 shows frequency distributions of valid matchups corresponding to each processor. To enable a fair performance intercomparison, we further identified common satellite matchups for the processors yielding equal number of samples.

3.4. Performance indicators

Here, we examine both linear and log-transformed metrics for evaluations of estimated (E) Chl*a* against that measured (M) *in situ*. The evaluation of all Chl*a* algorithms is carried out using an *in situ* validation set ($n > 1900$) independent of the training set ($n = 1000$). The performance metrics are as follows

$$RMSE = \left[\frac{\sum_{i=1}^{N}(E_i - M_i)^2}{n}\right]^{1/2} \ (\mathrm{mg/m^3}) \tag{5}$$

$$RMSLE = \left[\frac{\sum_{i=1}^{N}(\log_{10}(E_i) - \log_{10}(M_i))^2}{n}\right]^{1/2} \tag{6}$$

$$MAPE = 100 \times \tilde{r} \text{ where } \tilde{r} \text{ is the median of } [|E_i - M_i|/M_i] \text{ for } i = 1, \ldots, n \tag{7}$$

$$Bias = 10^{Z} \text{ where } Z = \left[\sum_{i=1}^{n}(log_{10}(E_i) - log_{10}(M_i))/n\right] \tag{8}$$

$$MAE = 10^{Y} \text{ where } Y = \left[\sum_{i=1}^{n}|log_{10}(E_i) - log_{10}(M_i)|/n\right] \tag{9}$$

where RMSLE is the root mean squared log-error, MAPE is the median absolute percentage error, Bias represents log-transformed residuals, and MAE stands for the mean absolute error computed in log-space. The latter (unitless) metrics computed in log-transformed space are believed to provide a better assessment of the algorithms owing to the log-normal distribution of Chl*a* data (Fig. 2) (O'Reilly and Werdell, 2019; Seegers et al., 2018). For instance, a Bias of 1.5 implies that Chl*a* estimations are, on average, 50% larger than those measured. In addition to the above metrics, we will also include slopes associated with the linear regression fits to facilitate comparisons with previously published results. Per recommendations in Seegers et al. (2018), we also conduct pair-wise comparisons to determine the Model Win Rate (MWR) expressed in %. Here, the residuals, i.e., $E_i - M_i$, per comparison (i) are assessed and % win across the entire validation set (n) is specified.

4. Results

4.1. Performance evaluation

The performance statistics on Chl*a* derived for simulated *in situ* R_{rs} shows that the MDN model outperforms Blend and OC for both MSI and OLCI spectral configurations (Fig. 5 and Table 2). For instance, RMSLE and Bias are improved nearly two-fold and by 20–40%, respectively. Also, MAPE suggests that MDN outperforms both OC and Blend over two-fold.

The scatterplots (Fig. 5) further indicate that OC3 and Blend lead to major overestimations for Chl*a* < 10 mg/m^3 and tend to underestimate in more eutrophic waters. Furthermore, the slope of the linear

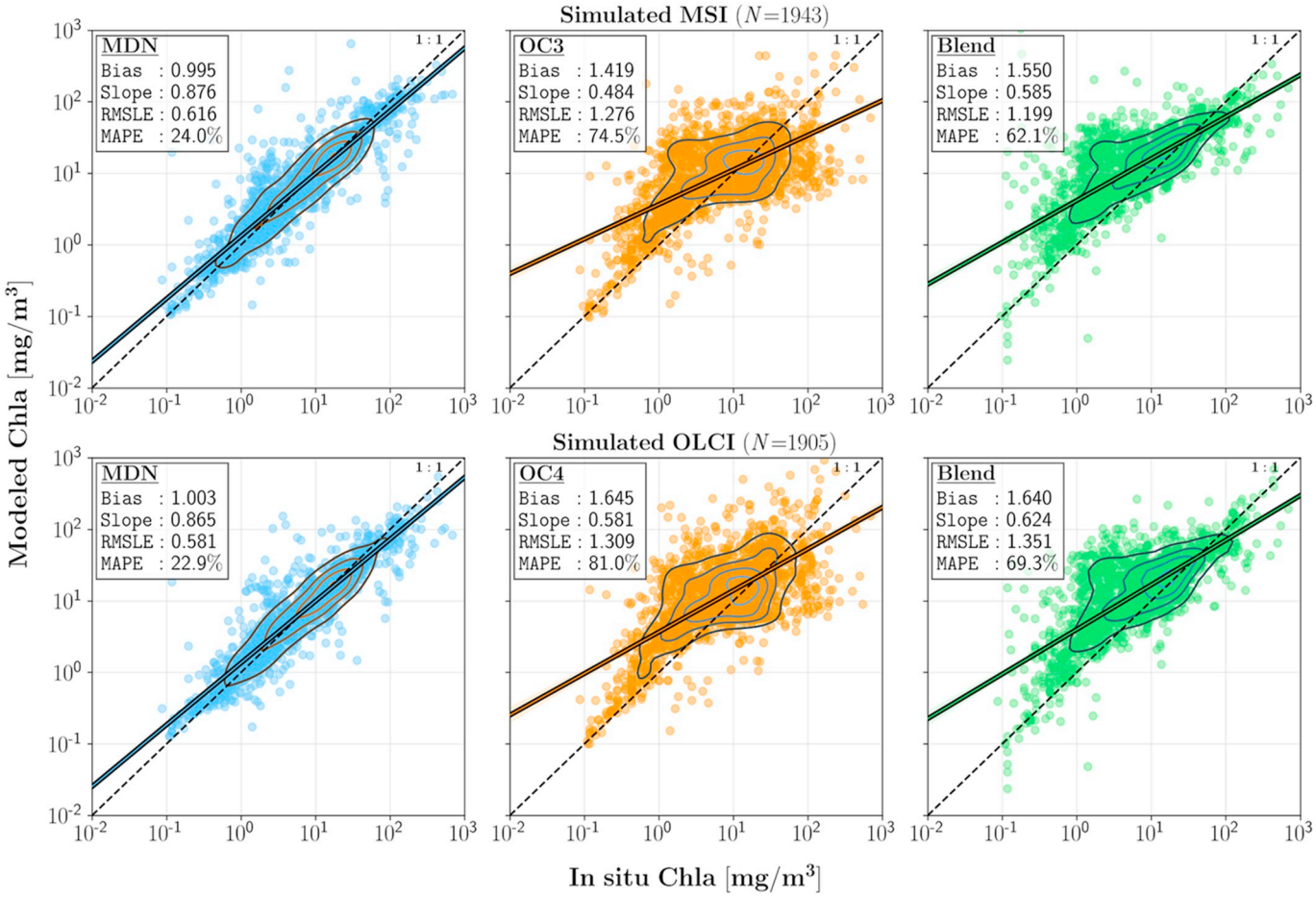

Fig. 5. Performance evaluation of Chl*a* retrievals using MDN, Blend and OC implemented for MSI- and OLCI-simulated *in situ* R_{rs} (Section 2). The contour plots indicate the density distributions. Further details on the overall and range-specific performances are included in Tables 2 and 3, respectively. A broader performance evaluation is available in Appendix A.

Table 2
Performance metrics associated with Chl*a* retrievals via MDN, OC, and Blend using >1900 co-located and coincident *in situ* R_{rs} – Chl*a* data pairs. Note that the Model Win Rate (MWR) is computed relative to MDN regarded as the reference model.

	RMSE (mg/m^3)	Slope	MAPE (%)	RMLSE	Bias	MAE	MWR (%)
			MSI (n = 1943)				
MDN	30.31	0.876	24.0	0.616	0.995	1.275	N/A
OC3	43.25	0.484	74.5	1.276	1.419	2.137	81.7
Blend	40.77	0.585	62.1	1.199	1.550	1.757	76.5
			OLCI (n = 1905)				
MDN	26.98	0.865	22.9	0.581	1.003	1.265	N/A
OC4	3364.6	0.581	81.0	1.309	1.645	2.221	82.7
Blend	31.66	0.624	69.3	1.351	1.640	1.867	77.1

regression fit to the log-transformed predicted versus observed Chl*a* relationships is closer to unity for the MDN model (>0.84) compared with the other models. This indicates the best fit across the entire concentration range. More statistical metrics are listed in Table 2. The MWR, in particular, suggests that in >70% of retrievals, MDN performs better than OC3 and Blend. The log-based absolute error (MAE) also indicates similar levels of improvements by MDN, i.e., ~28% less than that evaluated via Blend. The negligible Bias found for MDN-derived predictions further emphasizes significant increased accuracy in Chl*a* retrievals within a range covering three orders of magnitude. Note that the uneven validation sample size (1943 for MSI versus 1905 for OLCI) was due to a lack of full spectral coverage within the 400–800 nm range for a small subset of data (n = 38).

It is also important to underscore the relative performances of MDN for the spectral configurations of the two sensors. Evident from the statistical metrics tabulated in Table 2, it is inferred that the MDN model is able to generate Chl*a* products for MSI- and OLCI-like spectra with very similar precision and accuracy. This implies that MDN sufficiently retrieves most relevant information content associated with Chl*a* from the seven visible-NIR bands of MSI. In contrast, OC and Blend exhibit varying degrees of performances for simulated MSI and OLCI R_{rs} spectra.

The statistics tabulated in Table 3 for OLCI-simulated data further corroborate that the MDN model enhances Chl*a* retrievals across nearly all trophic states (Table 3). In particular, MDN significantly outperforms the other algorithms in waters with TSI ≤ 70 (i.e., Chl*a* ≤ 56 mg/m^3). In higher trophic states (TSI > 80), for which only 32 test samples are available, Blend and MDN appear to perform very similarly (Appendix A), suggesting that a larger sample size is required for a more rigorous assessment. Based on the estimated Bias in highly eutrophic waters (TSI ≥ 70), it is worthwhile noting that the three algorithms tend to underestimate Chl*a* suggesting the need for further improvements. Due to the similarities in the performances, corresponding MSI results are included only in the Appendix A (Table A.1). To gauge the performances for two broad categories of inland freshwaters and mixed coastal waters, we divided our validation dataset (of OLCI) into two groups, i.e., N = 1054 and N = 851 for inland and coastal waters, respectively. It was inferred that, on average, the performance of MDN is only marginally different for the two groups with RMSLE and slope

Table 3
Stratified performance assessment of MDN, OC4 (O'Reilly and Werdell, 2019), and Blend (Smith et al., 2018) for the OLCI-simulated data in TSI bins. The MDN model offers excellent enhancements in mesotrophic and eutrophic waters. The improvement is relatively small in comparison to Blend in hypereutrophic waters. For MWR computation, the win rate for each model is compared against MDN, i.e., OC4 = 78% implies that MDN leads to smaller residuals 78% of the times.

	OLCI	RMSE	Slope	MAPE	RMSLE	Bias	MAE	MWR
TSI ≤30 Chl*a* ≤ 0.94 (n=185) Median = 0.54 (mg/m^3)	MDN	1.47	0.76	29.3	0.64	1.22	1.29	NA
	OC4	5.77	1.30	119.5	1.38	2.19	2.19	80.7
	Blend	8.79	0.98	147.6	1.73	2.47	2.60	86.1
30 < TSI ≤ 40 0.94 < Chl*a* ≤ 2.6 (n=287) Median = 1.7 (mg/m^3)	MDN	4.13	1.09	29.5	0.75	1.15	1.37	NA
	OC4	25.78	0.71	262.3	1.79	3.62	3.65	91.0
	Blend	19.34	0.89	296.9	1.88	3.96	4.00	92.0
40 < TSI ≤ 50 2.6 < Chl*a* ≤ 6.4 (n=325) Median = 4.3 (mg/m^3)	MDN	13.10	0.92	27.4	0.64	1.11	1.30	NA
	OC4	25.11	0.43	138.1	1.31	2.38	2.45	87.1
	Blend	26.03	0.16	173.7	1.90	2.73	2.74	88.2
50 < TSI ≤ 60 6.4 < Chl*a* ≤ 20 (n=559) Median = 11.9 (mg/m^3)	MDN	7.40	0.85	18.7	0.40	0.97	1.20	NA
	OC4	34.92	0.19	52.0	0.86	1.22	1.74	76.6
	Blend	19.13	0.33	51.7	0.78	1.40	1.63	75.9
60 < TSI ≤ 70 20 < Chl*a* ≤ 56 (n=364) Median = 29.2 (mg/m^3)	MDN	12.80	1.11	19.5	0.43	0.87	1.21	NA
	OC4	488.23	1.10	54.9	0.99	0.77	1.89	78.9
	Blend	15.77	0.95	24.8	0.44	1.01	1.29	56.6
70 < TSI ≤ 80 56 < Chl*a* ≤ 154 (n= 153) Median = 88.2 (mg/m^3)	MDN	38.29	0.72	23.0	0.65	0.80	1.26	NA
	OC4	13665.06	1.45	76.4	1.80	0.33	3.50	89.6
	Blend	43.10	0.82	29.1	0.62	0.75	1.40	57.4
TSI > 80 Chl*a* > 154 (n=32) Median = 196 (mg/m^3)	MDN	202.40	0.43	44.4	1.02	0.55	1.79	NA
	OC4	526.26	0.22	94.0	2.34	0.15	8.33	88.5
	Blend	199.80	0.67	54.4	1.19	0.62	1.64	61.5

being 15% worse in inland waters.

A more extensive intercomparison with other widely used algorithms (e.g., 3-Band method in Moses et al. (2012)) is provided in the Appendix A (Table A.2). In general, except for MDN, no single algorithm offers a reasonable performance across the entire Chl*a* range. In particular, the 2-Band and 3-Band algorithms yield negative retrievals for a small portion of data with low Chl*a*, whereas NDCI (Mishra and Mishra, 2012) performs poorly for Chl*a* < 15 mg/m^3 and underestimates Chl*a* in more eutrophic waters. Negative retrievals obtained from these algorithms are expected as they are designed to operate in highly eutrophic waters by design.

4.2. Spatial integrity

To determine the viability of the MDN model for producing Chl*a* maps conforming to expert expectations, several OLCI and MSI images over three select regions in the U.S., including the Great Lakes, the lower Chesapeake Bay, and Lake Okeechobee (FL) were processed. The images representing a broad range of Chl*a* values were compensated for atmospheric effects using SeaDAS, POLYMER, and ACOLITE. For demonstration purposes, we only present visual intercomparisons of a handful of Chl*a* maps retrieved via POLYMER-derived R_{rs} products due to its proven performance demonstrated in Warren et al. (2019).

Fig. 6 illustrates OLCI- and MSI-derived Chl*a* products over the Great Lakes on April 30th, 2018 generated from near-simultaneous observations made by Sentinel-3A and Sentinel-2B. From the OLCI map, it is inferred that MDN produces realistic maps across a wide range of trophic levels, from oligotrophic waters of Lake Huron (Shuchman et al., 2013) to hypereutrophic waters of Lake Winnebago (Gons et al., 2008). Although cross-mission product consistency requires long-term, rigorous analyses of products, the MDN model shows promise in generating interconsistent Chl*a* products. Fig. 7 further compares Chl*a* products over the lower Chesapeake Bay area (March 27th, 2019), where spring blooms commonly occur (Marshall et al., 2006). Historically, seasonal algal blooms (e.g., dinoflagellate *Prorocentrum minimum*) have been recorded in the lower York River, the James River, and at their mouths (Marshall, 1994; Marshall, 1996). It is inferred that the MDN model successfully produces Chl*a* products ranging from 4 to 50 mg/m^3. Major differences between MDN- and Blend-derived products are indicated in the maps, where larger gradients are identified in MDN products in the James River. Given the superior performance of MDN within the Chl*a* < 10 mg/m^3 range (Fig. 5), MDN is expected to capture such abrupt changes.

Additionally, we examine the performances for another MSI image (June 5th, 2019) over Lake Okeechobee (FL) in Fig. 8. This shallow lake, rich in near-surface sediment concentrations, has lately

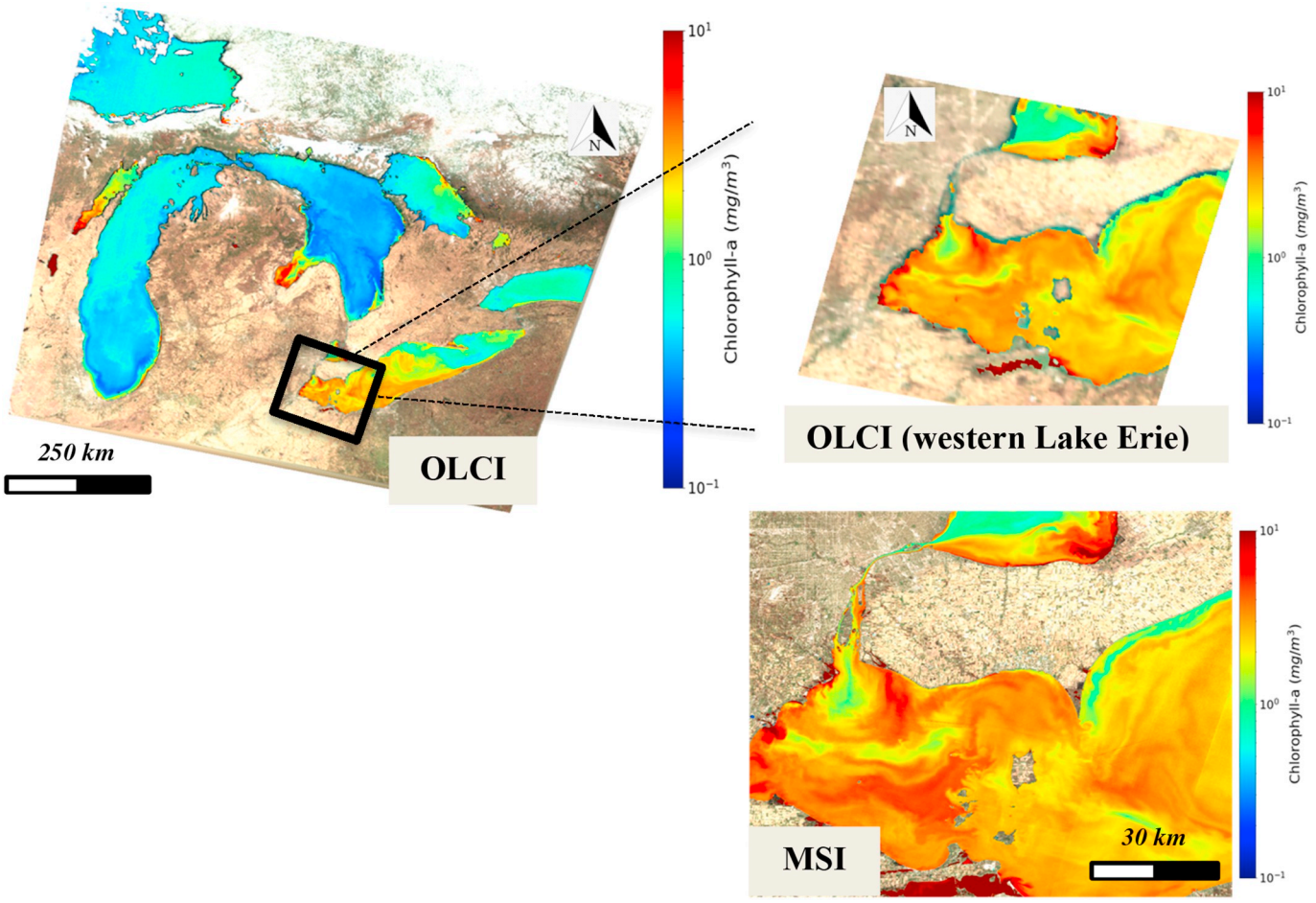

Fig. 6. OLCI- and MSI-derived Chla products over the Great Lakes and the western basin of Lake Erie for near-coincident overpasses of Sentinel-3A and Sentinel-2B on April 30th, 2018.

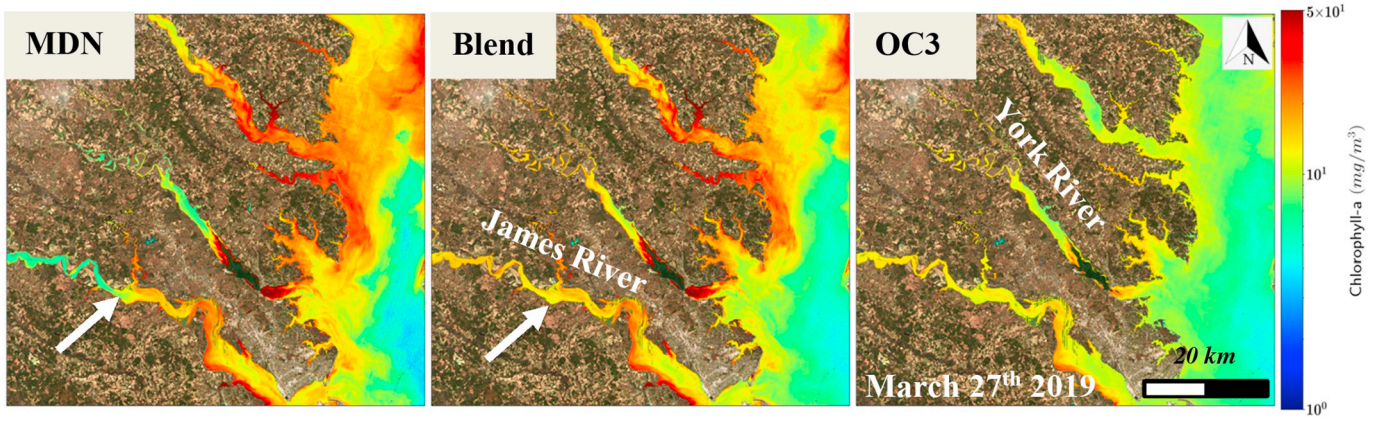

Fig. 7. MSI-derived Chla products estimated via MDN, Blend, and OC3 algorithms over the lower Chesapeake Bay (VA), March 27th, 2019. The TOA MSI image was processed to R_{rs} using POLYMER.

experienced seasonal cyanobacteria blooms from early May to late September (Metcalf et al., 2018; Williams et al., 2001). The three algorithms capture the spatial variability of the cyanobacteria bloom across the lake and provide similar Chl*a* retrievals (Chl*a* < 1.5 mg/m^3) on the eastern coasts of Florida. An *in situ* measurement, made approximately 1 h after a Sentinel-2 overpass at the marked location, has reported Chl*a* = 10.1 mg/m^3, which is closely estimated by MDN and OC3, i.e., 12.9 and 10.9 mg/m^3, respectively, and overestimated by Blend by 80%.

4.3. Impact of atmospheric correction

It is essential to assess the sensitivity of the MDN model to different AC processors and gain further insights into how uncertainties in this process propagate to Chl*a* products. Fig. 9 illustrates MDN-derived Chl*a* for a single example of an MSI image over the lower Chesapeake Bay processed via SeaDAS (v7.5), POLYMER (v4.11), and ACOLITE (20190326.0). Despite the fact that the relative spatial distributions of MDN-derived Chl*a* are, in general, retained through the three processors, there are clearly differences in the magnitude of Chl*a*. For

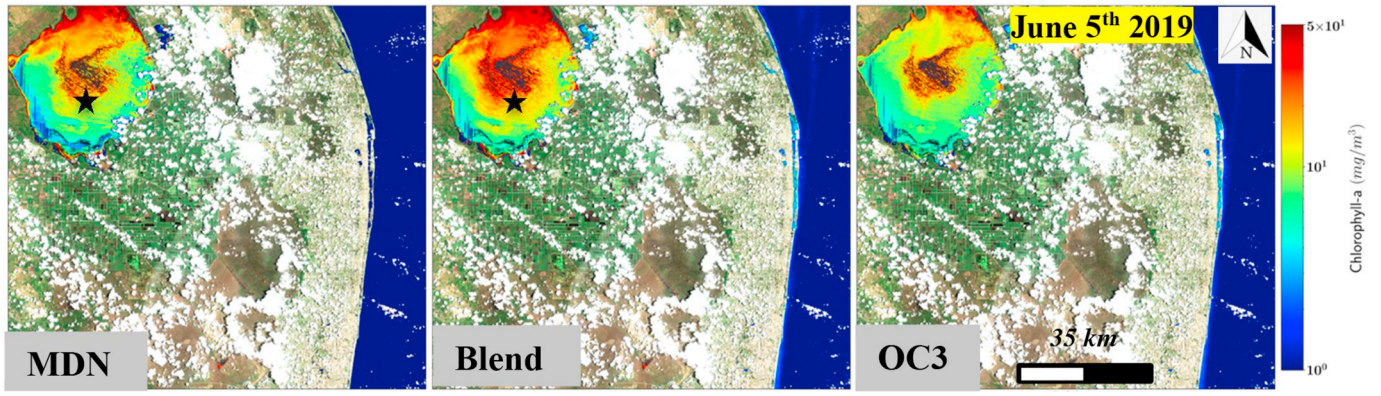

Fig. 8. MSI-derived Chla products over Lake Okeechobee (June 5th, 2019). The POLYMER processor was adopted to generate R_{rs} products. Near-concurrent *in situ* Chla measurement at the location indicated is reported 10.1 mg/m^3 (https://www.waterqualitydata.us).

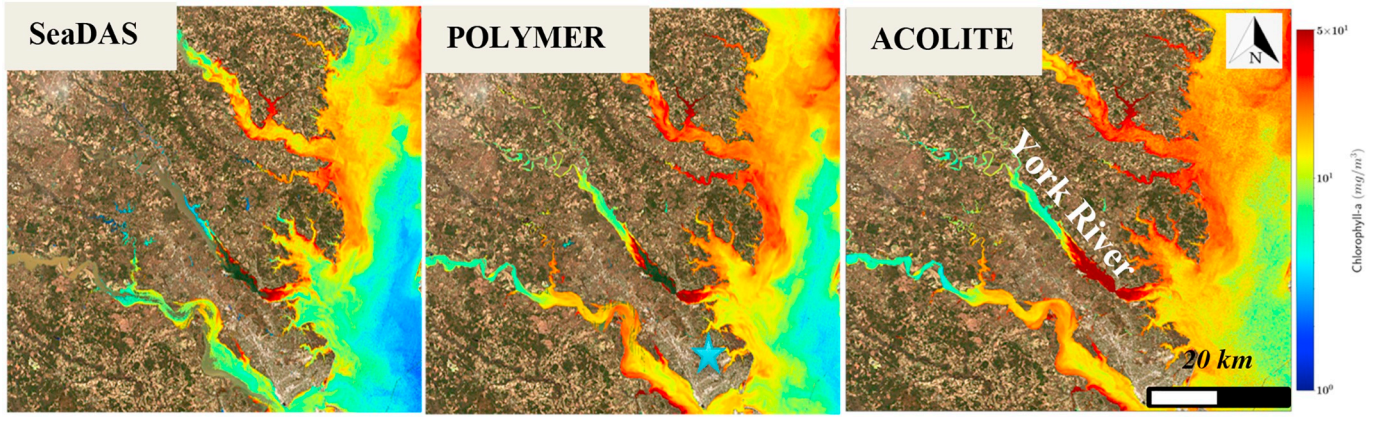

Fig. 9. MDN-derived Chl*a* products obtained from three different AC processors over the lower Chesapeake Bay as imaged by MSI on March 27th, 2019. The mean daily aerosol optical thickness at 500 nm at the marked location (middle panel) was estimated to be 0.047. The measurement was made at NASA's Langley Research Center, a station that belongs to the AErosol RObotic NETwork (AERONET) (Holben et al., 1998).

example, the SeaDAS-processed map shows lower Chl*a* values than the others. Moreover, ACOLITE allows retrievals in a hypereutrophic reach of the York River, where both SeaDAS and POLYMER fail to retrieve valid products. While valid retrievals do not necessarily warrant viable R_{rs} products (as elaborated below), distinct products from the three processors for this example with a low aerosol loading, i.e., daily averaged aerosol optical thickness of 0.047 at 500 nm measured at NASA's Langley Research Center of the Aerosol Robotic Network; (Holben et al., 1998), verify the challenging task of AC and its effects on downstream products.

To further elucidate the reason for such differences, we quantify the quality of satellite-derived map products processed via SeaDAS, POLYMER, and ACOLITE. Fig. 10 illustrates the MSI matchup results. As denoted in Section 3.3, due to different quality-assurance schemes, different numbers of valid matchups are obtained for the AC processors. The assessments based on identical numbers of matchups are also shown in Fig. 12. From Fig. 10, it is evident that the excellent performance of MDN (Section 4.1) is majorly affected by the AC, leading to varying degrees of biases or random noise. Nevertheless, statistically, the MDN model outputs Chl*a* values that better represent *in situ* measurements. The MDN-derived values processed through POLYMER better resemble those processed via SeaDAS, albeit POLYMER appears to retrieve Chl*a* under more challenging atmospheric conditions, i.e., POLYMER has produced ~70% more valid matchups, and thus, exhibits more noisy retrievals. ACOLITE-based Chl*a* values, on the other hand, demonstrate major biases (overestimation) across the entire range, which aligns with maps shown in Fig. 9. Predicted Chl*a* by OC3 and Blend are found consistently biased high for the three processors, which could be attributed to the sensitivity of the OC algorithms to the presence of non-algal particles or CDOM in the Chesapeake Bay (Tzortziou et al., 2007). Further, it is also evident that the OC3– and Blend-derived Chl*a* products when SeaDAS-generated R_{rs} products are supplied are highly scattered. This is because of the noisy observations in the NIR and SWIR bands (Section 3.2) that affect R_{rs} products in the visible or other NIR bands (Pahlevan et al., 2017b). Overall, although the matchup datasets are not as representative as the development data (Section 2), the performance (Fig. 10) within the $1 < \text{Chl}a < 10$ mg/m^3 range is in agreement with those illustrated in Fig. 5, i.e., both OC3 and Blend tend to overestimate within this range. Further, OC3 and Blend models seem to output more reasonable retrievals when applied to POLYMER-based data compared to those derived from SeaDAS, although MDN is found to significantly outperform these algorithms.

The results for the OLCI-A-derived Chl*a* matchup analysis are shown in Fig. 11. Despite the differences in the number of matchups, similar conclusions as for MSI can be drawn for OLCI-A. That is, SeaDAS-based band-ratio products are slightly more scattered than those produced via MDN, and all the three Chl*a* algorithms show varying levels of overestimations. This overestimation is ~36% in the MDN-derived Chl*a* produced by POLYMER; however, OC3 and Blend products exhibit much higher biases in retrievals. Analogous to the MSI assessments, these observations are in line with the validation results (Fig. 5), i.e., OC4 (O'Reilly and Werdell, 2019), and Blend primarily predict higher Chl*a* values within the $1 < \text{Chl}a < 10$ mg/m^3 range for which the Chesapeake Bay data are most representative. Overall, the statistics and the scatterplots suggest that POLYMER-derived R_{rs} allows for more Chla predictions when MDN is utilized. Fig. 12 illustrates the common Chl*a*

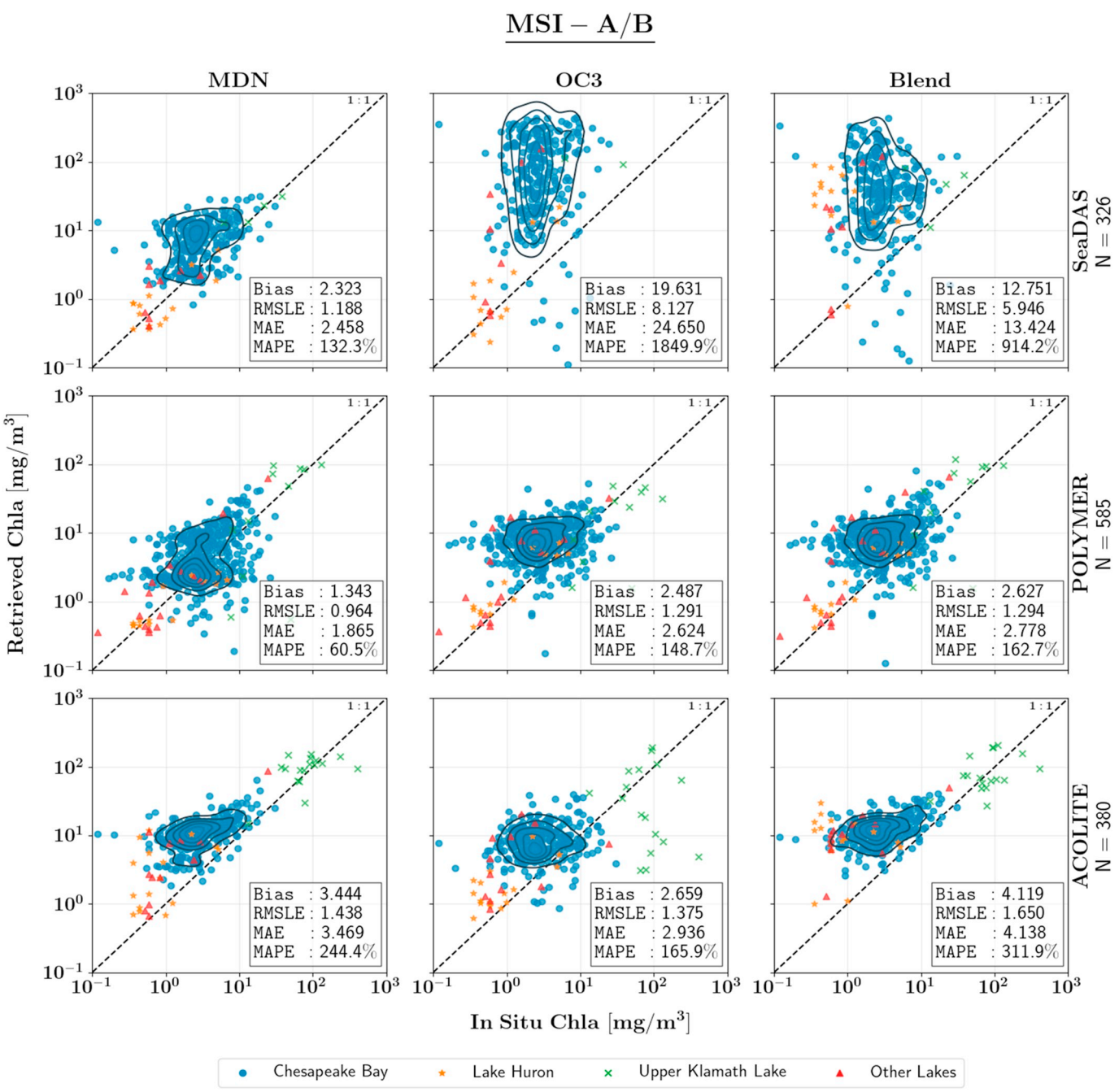

Fig. 10. MSI-A/B matchup analysis of Chl*a* products derived from different processors and algorithms. More than >85% of matchups originate from autonomous measurements made at buoys deployed in the Chesapeake Bay. Other lakes include Lake Simcoe, Lake Ontario, Lake Erie, Lake Superior, and Lake Winnipeg.

matchup products (produced via MDN only) for each sensor (281 for MSI-A/B and 219 for OLCI-A).

Although scatterplots suggest similar performances for SeaDAS and POLYMER, similar to Figs. 10 and 11, POLYMER, on average, provides products with lower uncertainties as evidenced by all the error metrics, i.e., 10–30% improvements relative to other processors. ACOLITE, on the other hand, appears to output biased high Chl*a* products. The reason behind such biases may be explained by inspecting Fig. A.1 (Appendix), where normalized frequency distributions of select bands (R_{rs}(490), R_{rs}(560), and R_{rs}(705)) that contribute most to Chl*a* retrievals are illustrated. For MSI, it can be seen that the ACOLITE R_{rs} retrievals are largest across the visible and NIR bands, whereas SeaDAS-derived R_{rs} in the blue and green bands skewed towards lower values. In general, elevated retrievals of R_{rs}(709) (Gitelson et al., 2007) or underestimations in R_{rs}(490) and R_{rs}(560) can both lead to over-predictions of Chl*a* (Stumpf and Tyler, 1988). For OLCI, notable differences between SeaDAS and POLYMER are found *only* in R_{rs}(490). These observations for SeaDAS products likely imply errors in the extrapolation into the blue region of the spectrum or a limited representativeness of aerosol models applied (Pahlevan et al., 2017a).

Fig. 13 further shows a few instances of Blend- and OC3-derived products that lack consistency in their spatial patterns when processed via POLYMER and SeaDAS. The main artifact highlighted corresponds to the sudden change in MSI's viewing azimuth angle between adjacent detector modules (Pahlevan et al., 2017b; Pahlevan et al., 2017c) with one looking away from the sun and the other looking towards the sun giving out different reflected radiances from the water surface or from thick aerosol layers, i.e., haze. This slight difference yields residual

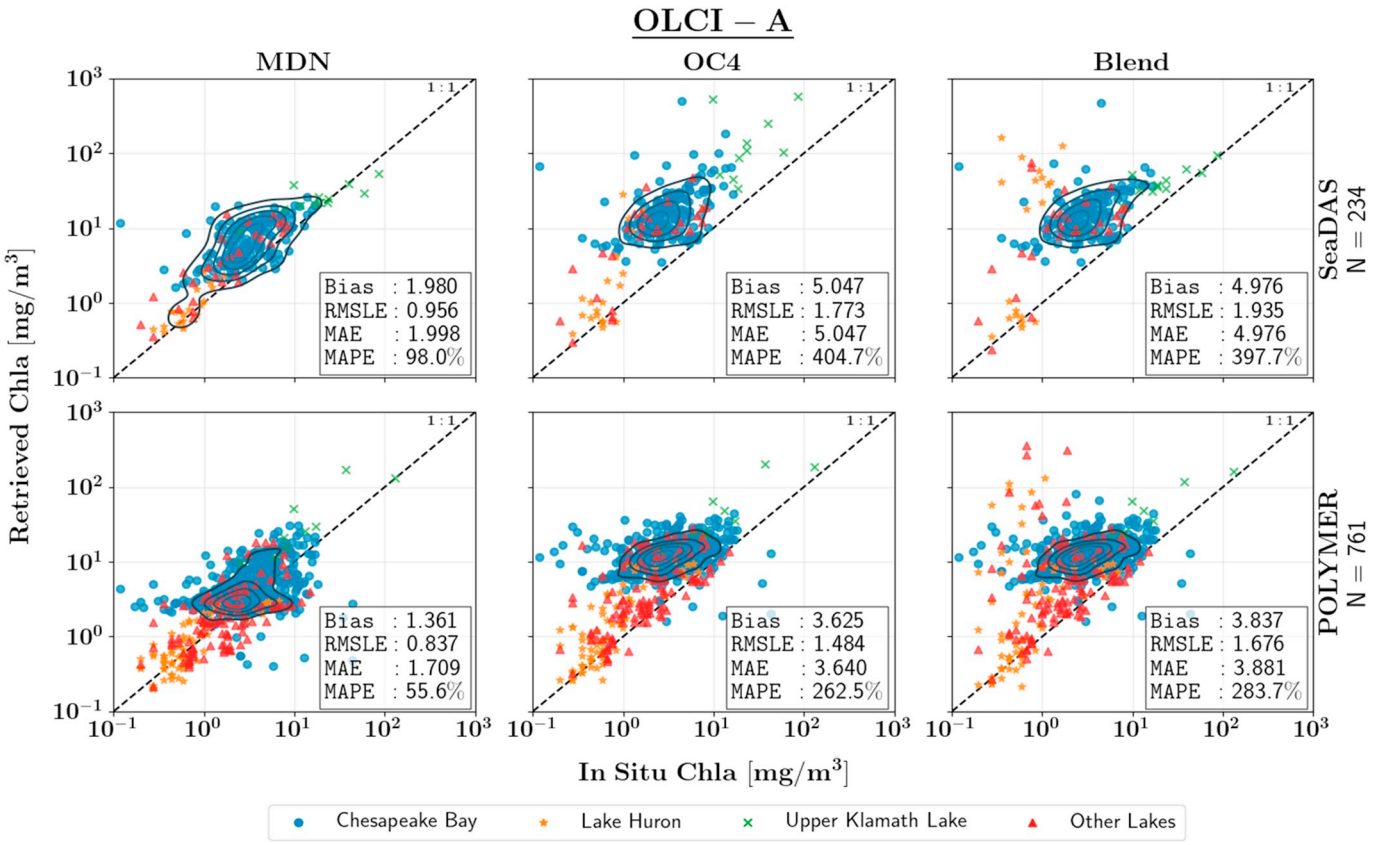

Fig. 11. OLCI-A Chl*a* matchups processed via two AC methods and generated by MDN, OC4 (O'Reilly and Werdell, 2019), and Blend (Smith et al., 2018). Given the statistical indicators (Section 3.4), MDN when processed via POLYMER provides better predictions than those from OC4 and Blend. Other lakes include Lake Simcoe, Lake Ontario, Lake Erie, Lake Superior, and Lake Winnipeg.

differences in R_{rs} products, which may differ from one band to the other. We speculate that because MDN utilizes all the available spectral bands for Chl*a* predictions, it is less susceptible to these noise sources. In contrast, Blend and OC3 both rely on ratios of two or three bands that may amplify the residual differences between the detector modules.

5. Discussion

Here, with a sizeable *in situ* dataset, originating from several regions inclusive of diverse biogeochemical conditions, we demonstrated that the MDN model is a viable solution for Chl*a* estimation. The semi-global nature of *in situ* data suggests its potential utility for global mapping of Chl*a* in inland and nearshore coastal waters for combined Sentinel-2 and -3 observations with near-daily revisit frequency.

5.1. Development dataset

Although this large database compiled through an ad-hoc, community-wide data sharing activity enabled a comprehensive testing of the MDN model, there are evidently concerns about inconsistencies in measurement/sampling techniques, the instrumentation and their corresponding calibration/performances, and how such differences reflect in algorithm development and validation. On one hand, ideally, radiometric data should be collected via well-calibrated instruments and community-accepted protocols with a unified processing technique (Ruddick et al., 2019). Nevertheless, relaxing such stringent requirements likely enables a more robust algorithm development and validation for a wider range of trophic conditions, which is what has been adopted in this study. On the other hand, although our first-order correction for pheophytin and other pigments appeared to improve the quality of uncorrected *in situ* Chl*a* measurements, the preferred method for *in situ* Chl*a* is the High Pressure Liquid Chromatography (HPLC) (Roesler et al., 2017). Future coordinated field exercises may guarantee high-quality datasets for algorithm design and assessment.

5.2. MDN model

Compared to traditional NNs, this class of NN helps overcome the non-unique characteristic of the solution to the inverse problem of retrieving Chl*a* using likelihoods generated in the training and validation steps. When tested globally for its rigor, the MDN model, trained with all the available data (n = 2943), can be adopted for generating long-term Chl*a* products from high-quality R_{rs} climate records (Mélin et al., 2017) in inland and nearshore coastal waters. Robust retrospective Chl*a* products will enable precise determination of baseline Chl*a* for long-term assessments of eutrophication in global waterbodies. Yet, its performance for missions lacking spectral bands within the 700–800 nm range should be thoroughly examined. While we find that MDN outperforms most state-of-the-art algorithms, the uncertainties put forth in Tables 2 and 3 further signify the need for improving MDN performance. This may be achieved by simultaneously retrieving other water quality parameter (e.g., TSS) and IOPs. As the implemented MDN model learns the full covariance matrix between outputs, having these quantities learnt concurrently with the true target improves estimates where the input R_{rs} may be ambiguous. Moreover, like any other machine learning algorithm, the accuracy of MDN is subject to the distribution of field data and their uncertainties; hence, its performance can be much improved with data acquired using a unified measurement approach. For instance, although the maximum Chl*a* value in our development data is 1209 mg/m^3, the data distribution is quite sparse for Chl*a* > 90 mg/m^3, limiting the utility of MDN in waters whose Chl*a*

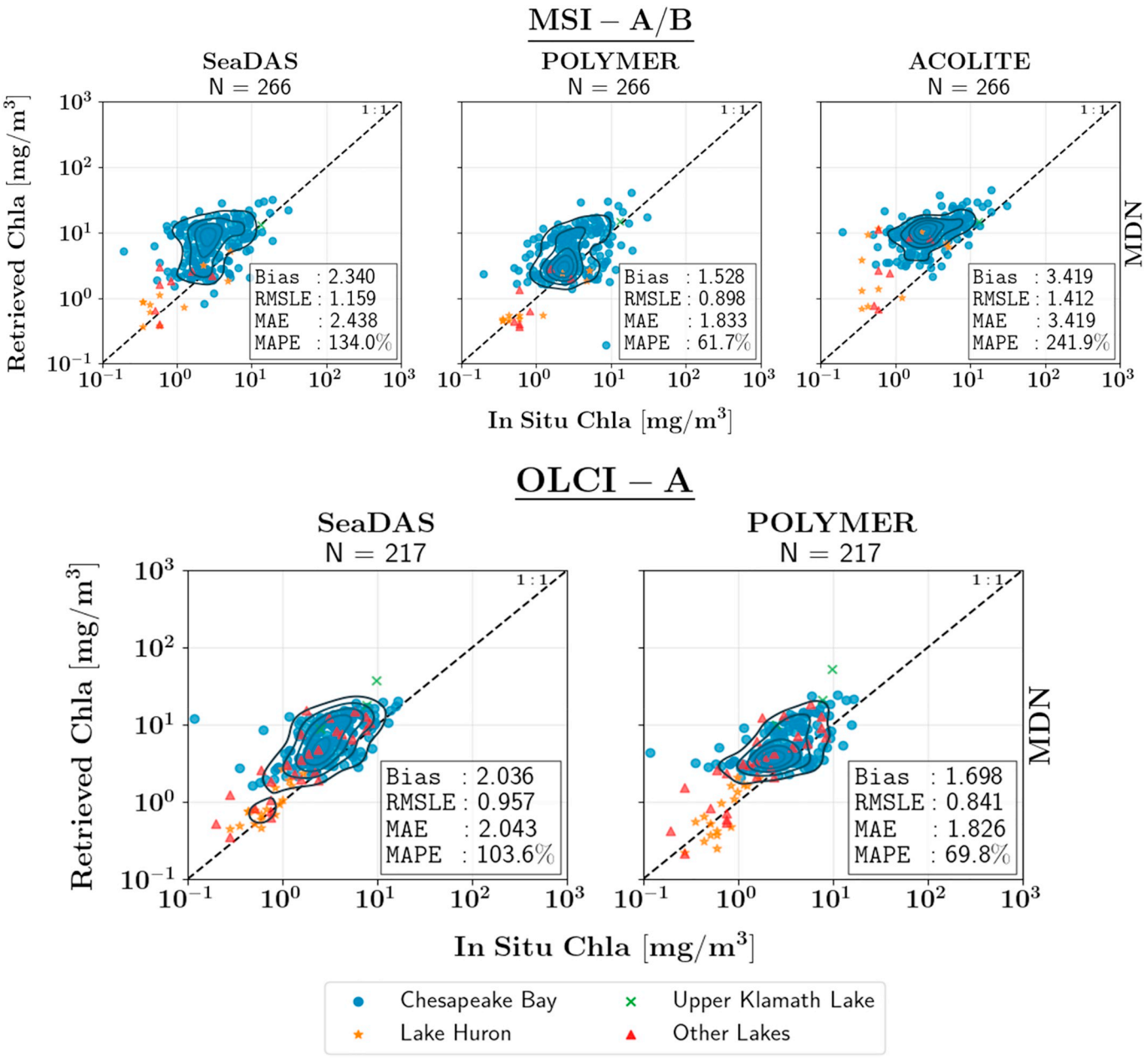

Fig. 12. MDN-derived Chla retrievals for common matchups processed via SeaDAS, POLYMER, and ACOLITE for 291 MSI-A/B and 218 OLCI-A images.

magnitudes exceed this threshold (Section 4.1). Recognizing strong correlations between band-ratio indices and Chl*a*, one may attempt to supplement the input feature space with other features. However, in practice, these band-ratio features may not enhance Chl*a* estimations; rather, they may lead to instability in the network induced by image-derived, near-zero R_{rs} retrievals in ratio denominators, and thus, extremely large model inputs. In addition, as shown in Section 4.2, the model performance is impacted by the uncertainties in R_{rs}, verifying that the model is predictable and behaves as expected, i.e., inaccurate inputs yield incorrect outcomes. Further examination of model behavior and its sensitivity to various degrees of random or systematic noise as well as to the choice of input bands should be considered in future research efforts.

5.3. Map products and atmospheric correction

In spite of its remarkable performance (Bias = 1.0, RMSLE <0.6 and MAE < 1.3) with respect to other existing algorithms (Section 4.1), the MDN performance is hampered by the suboptimal removal of atmospheric effects (Section 4.2). Although the matchup database was not as substantial as that used in the algorithm development and validation (in terms of both size and representativeness; e.g., $>88\%$ of MSI matchups evaluated via POLYMER lies within the 1–15 mg/m^3 range), our results indicate that, no matter how robust an algorithm is, the atmospheric correction can constrain the ability to retrieve Chl*a*. Although one should note that the apparent retrieval uncertainty will also be driven partly by the inherent difficulties in acquiring reliable matchups in highly dynamic inland and coastal waters, where large spatial (Pahlevan et al., 2016) and temporal variability in Chl*a* may exist. Furthermore, we find that the MDN model when supplied with POLYMER-derived R_{rs} products allows for better predictions than those by other models or processors and enables more retrievals (Zhang et al., 2018). This, nevertheless, may not warrant high-fidelity products for scientific studies as reflected in Figs. 10 and 11, where outliers can evidently be found. In fact, relatively large errors (Figs. 10 and 11) indicate that these products may be impracticable when high-quality

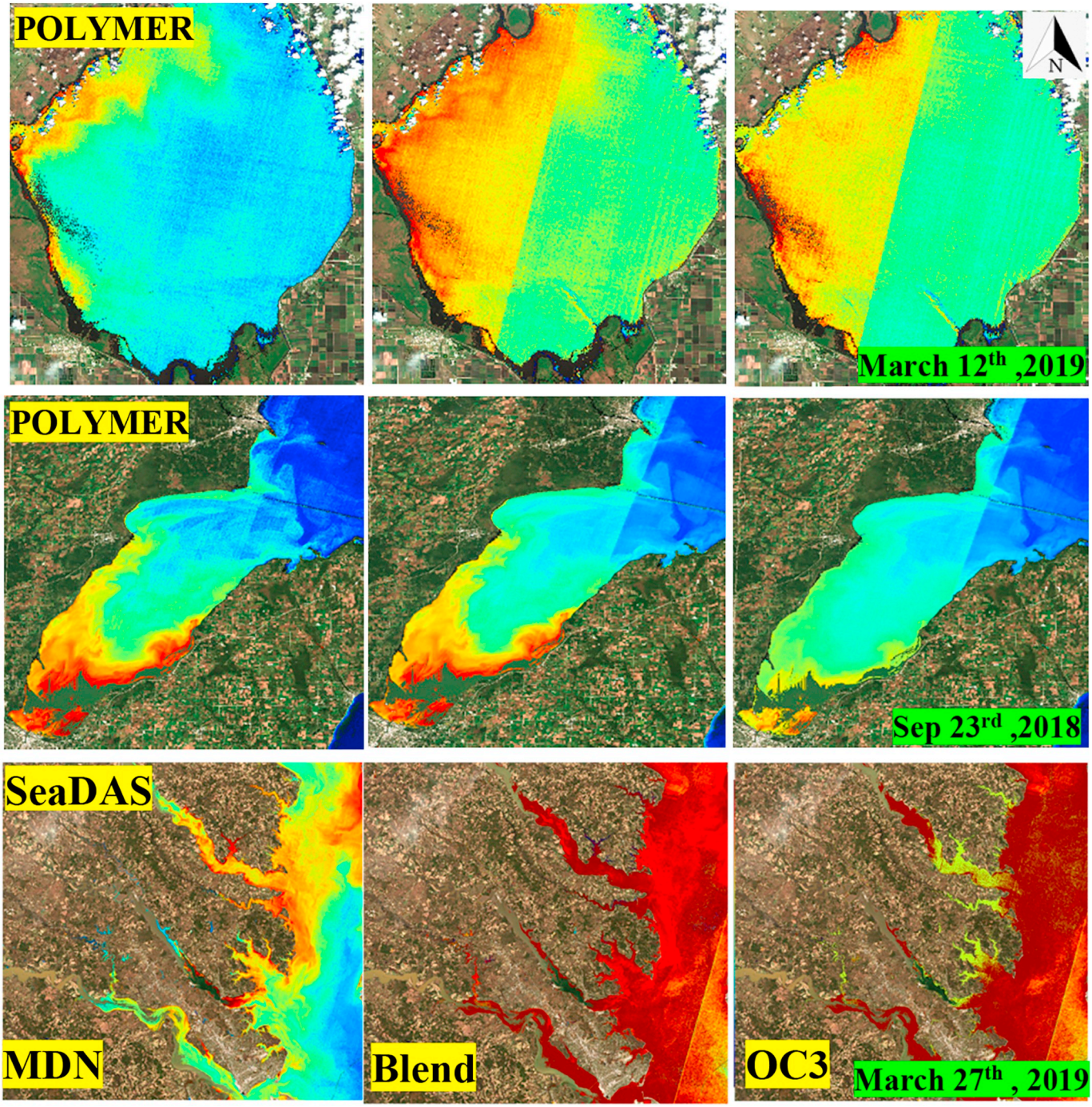

Fig. 13. Sensitivity of MDN, Blend and OC3 to imaging schemes and uncertainties in R_{rs} products for MSI images. The MDN-derived Chla maps (left column) are less sensitive to image artifacts present in products obtained from both POLYMER (top and middle rows) and SeaDAS (bottom row). Note that MDN leverages all valid R_{rs} measurements while Blend and OC3 use only select bands.

science products are desired. In highly eutrophic waters, for instance, POLYMER appears to be limited, likely due to the overly simplified in-water model used in the polynomial fitting scheme (Steinmetz et al., 2011).

Although limited in retrieving valid R_{rs} in a wide range of conditions (Warren et al., 2019), SeaDAS shows promising Chl*a* retrievals via the MDN model. Band-ratio-based products derived, in particular from MSI, should, however, be utilized with caution (Figs. 10, 12, and 13). The low signal-to-noise-ratio of the NIR and SWIR bands of MSI yields noisy band-ratios in Rayleigh corrected radiance space. Through aerosol model selection and extrapolations, this noise is propagated to visible bands, increasing the overall noise in R_{rs} products (Pahlevan et al., 2017a; Pahlevan et al., 2017b). Since OLCI's radiometric performance is better suited for ocean color applications (Donlon et al., 2012), this issue is less pronounced in the respective products and can be further minimized through spatial filtering, which was not applied in this study (Section 3.3). In addition, Chl*a* products obtained via all processors over the Chesapeake Bay showed major biases. Since these biases are, to some extent, reduced in POLYMER-based products, adjacency effects may contribute to these uncertainties (Bulgarelli et al., 2014); although more research is required to corroborate this speculation as the lack of representative aerosol models (Pahlevan et al., 2017a) and/or

uncertainties in the extrapolations into the blue bands in SeaDAS processing (Ibrahim et al., 2019) may introduce additional uncertainties (see Fig. A.1). Although the Blend algorithm applies a weighting scheme to retrieve Chl*a* for a broad span of trophic conditions, our matchup assessments indicate that after implementing the AC, its performance degrades significantly in less eutrophic waters (Chl*a* < 1 mg/m^3) for both sensors (Figs. 10 and 11). In particular, Blend-derived matchups from OLCI (Fig. 11) exhibits larger scatter compared to that from OC4. This loss in performance was also observed (not shown here) in map products of nearshore areas of the Great Lakes. While ACOLITE exhibited biases within the most representative Chl*a* range (Chl*a* < 15 mg/m^3), the DSF scheme tends to provide more valid, and likely better, Chl*a* estimates in hypereutrophic waters, i.e., the Upper Klamath matchups with Chl*a* > 70 mg/m^3, when MDN and Blend are utilized. Given the quality of MSI products generated via SeaDAS, the SWIR-based AC available in ACOLITE should certainly be avoided. Out of the three AC processors evaluated, currently only SeaDAS produces uncertainties associated with R_{rs} products. In particular, POLYMER, which permits retrievals even under thin clouds, should inform per-pixel uncertainties to assure availability of confidence metrics in downstream products.

Despite the fact that this study assessed only a handful of AC processors, the atmospheric correction appears be a major obstacle in remote estimations of Chl*a* through the MDN model, leading to at least 30% loss of performance (Sections 4.1 and 4.2). Therefore, for potentially a more rigorous retrieval of Chl*a*, a machine-learning method like MDN may be trained with TOA or Rayleigh-corrected reflectance matchups as input (Binding et al., 2011; Matthews et al., 2012). One may also infer water type from TOA or Rayleigh-corrected reflectances and then decide on applying an appropriate AC, though this scheme may result in artifacts in map products and a blending approach may be inevitable. Alternatively, a machine-learning model may be prescribed with retrieved R_{rs} to learn the corresponding noise in the data, i.e., supply the model with realistically perturbed R_{rs}. Future studies should also extend the matchup analysis provided here (Section 4.2) as our assessments were primarily limited to Chl*a* <15 mg/m^3, measured in the Chesapeake Bay; consequently, the conclusion drawn from the matchup analysis may *not* be generalized.

6. Conclusion

This manuscript presents a novel machine-learning algorithm (MDN) applied to the inverse problem of retrieving Chl*a* from R_{rs} for Sentinel-2 (MSI) and Sentinel-3 (OLCI) observations. Using a set of coincident *in situ* Chl*a* – R_{rs} measurements (n = 2943) made over a diverse range of bio-optical regimes, the algorithm is trained, substantiated, and compared against state-of-the-art, community-accepted algorithms. We demonstrate that the MDN model works equally well for both MSI and OLCI data (Bias = 1.0, MAE < 1.28, and RMSLE <0.62), suggesting its potential in producing seamless high-quality Chl*a* products. As evidenced through image and satellite matchup analyses (n < 800), the MDN model generates realistic spatial distributions and produces most accurate Chl*a* map products, though we find that the model is sensitive to uncertainties in R_{rs} products. The lowest errors for MSI products based on our matchups include Bias = 1.34, MAE = 1.86, and RMSLE = 0.96, signifying the atmospheric correction as the main hurdle in generating high-quality Chl*a* products. Further research should be directed towards global assessments of MDN applied to R_{rs} products from various atmospheric correction processors (Doxani et al., 2018) as well as towards further expansion and standardization of *in situ* data collection methods. Moreover, because MDN learns the covariances among target variables, the model performance is expected to be enhanced via simultaneous retrievals of various in-water parameters of interest, i.e., Chl*a*, TSS, IOPs, etc. Subject to a widespread corroboration of its potential, MDN implementation can be extended to other optical remote sensing data as a pathway to move one step closer towards producing seamless multimission Chl*a* products using a single algorithm over inland and coastal waters. Constructing such harmonized products, nonetheless, may be hampered by complexities introduced by inherent differences in remote-sensing observations and inconsistencies in the atmospheric corrections. Hence, space agencies and satellite operation organizations should elevate inter-agency/international coordination to maximize the utility of joint constellations prior and during the mission lifetimes.

Contribution

Nima Pahlevan: Conceptualization; Brandon Smith, John Schalles, Caren Binding, Zhigang Cao, Ronghua Ma, Krista Alikas, Kersti Kangro, Daniela Gurlin, Nguyễn Hà, Bunkei Matsushita, Wesley Moses, Steven Greb, Moritz K. Lehmann, Michael Ondrusek, Natascha Oppelt, Richard Stumpf: Data curation; Brandon Smith: Formal analysis; Nima Pahlevan:Funding acquisition; Nima Pahlevan and Brandon Smith: Investigation; Brandon Smith: Methodology; Nima Pahlevan: Project administration; Nima Pahlevan: Resources; Brandon Smith: Software; Nima Pahlevan: Supervision; Brandon Smith: Validation; Brandon Smith: Visualization; Nima Pahlevan and Brandon Smith: Roles/Writing - original draft; Nima Pahlevan: Writing - review & editing.

Declaration of competing interest

The authors declare that they have no known competing financial interests or personal relationships that could have appeared to influence the work reported in this paper.

Acknowledgement

The algorithm development, the implementation, and the analyses were funded under NASA ROSES Awards #80NSSC18K0077, #80HQTR19C0015, and the USGS Landsat Science Team Award #140G0118C0011. We further appreciate dedicated review notes provided by two anonymous reviewers assisting in improving the overall quality of this manuscript.

Appendix A

In what follows, a few widely used Chl*a* algorithms implemented for intercomparison purposes are listed. Furthermore, the categorical performance analyses for MDN, OC3, and Blend implemented to MSI-like R_{rs} are provided in Table A.1. The overall statistical analyses associated with the performances of all the algorithms are also tabulated in Table A.2.

OC2 (MSI) (O'Reilly and Werdell, 2019):

$$x = log_{10}[\,R_{rs}(492) * R_{rs}(560)^{-1}$$
$$y = 0.2389 - 1.9369x + 1.7627x^2 - 3.0777x^3 - 0.1054x^4$$
$$Chl_{OC2} = 10^y \quad \text{(A.1)}$$

OC3 (MSI) (O'Reilly and Werdell, 2019):

$$x = log_{10}[\,(max\,[R_{rs}(442), R_{rs}(492)]) * R_{rs}(560)^{-1}\,]$$
$$y = 0.3308 - 2.6684x + 1.5990x^2 + 0.5525x^3 - 1.4876x^4$$
$$Chl_{OC3} = 10^{y} \tag{A.2}$$

OC4 (OLCI) (O'Reilly and Werdell, 2019):

$$x = log_{10}[\,(max\,[R_{rs}(442), R_{rs}(490), R_{rs}(510)]) * R_{rs}(560)^{-1}\,]$$
$$y = 0.4254 - 3.2168x + 2.8691x^2 - 0.6263x^3 - 1.0933x^4$$
$$Chl_{OC4} = 10^{y} \tag{A.3}$$

OCx (MSI) (O'Reilly and Werdell, 2019):

$$CI = R_{rs}(560) - (0.473 * R_{rs}(442)) - (0.527 * R_{rs}(665))$$
$$Chl_{CI} = 10^{-0.4909+191.6590*CI} \quad [CI \le -0.005\ sr^{-1}]$$
$$w = (Chl_{CI} - 0.15)/(0.20 - 0.15)$$
$$Chl_{OCx} = \{$$
$$Chl_{CI} \quad [Chl_{CI} \le 0.15\ mg\ m^{-3}\,]$$
$$Chl_{OC3} \quad [Chl_{CI} > 0.20\ mg\ m^{-3}\,]$$
$$w * Chl_{OC3} + abs(w-1) * Chl_{CI} \quad [0.15 < Chl_{CI} \le 0.20\ mg\ m^{-3}\,]$$
$$\} \tag{A.4}$$

OCx (OLCI) (Hu et al., 2012; O'Reilly and Werdell, 2019):

$$CI = R_{rs}(560) - (0.473 * R_{rs}(442)) - (0.527 * R_{rs}(665))$$
$$Chl_{CI} = 10^{-0.4909+191.6590*CI} \quad [CI \le -0.005\ sr^{-1}]$$
$$w = (Chl_{CI} - 0.15)/(0.20 - 0.15)$$
$$Chl_{OCx} = \{$$
$$Chl_{OC4} \quad [Chl_{CI} > 0.20\ mg\ m^{-3}\,]$$
$$w * Chl_{OC4} + abs(w-1) * Chl_{CI} \quad [0.15 < Chl_{CI} \le 0.20\ mg\ m^{-3}\,]$$
$$\} \tag{A.5}$$

2-Band (Moses et al., 2012):

$$Chl_{2Band} = (35.75 * R_{rs}(708)/R_{rs}(665) - 19.3)^{1.124} \tag{A.6}$$

3-Band (Moses et al., 2009b):

$$Chl_{3Band} = 232.329 * (R_{rs}(665)^{-1} - R_{rs}(708)^{-1}) * R_{rs}(753) + 23.17 \tag{A.7}$$

Blend (Smith et al., 2018):

$$r = R_{rs}(708)/R_{rs}(665)$$
$$phi = \{$$
$$0.75 \quad [\,r < 0.75\,]$$
$$1.15 \quad [\,r > 1.15\,]$$
$$r \quad [\,0.75 \le r \le 1.15\,]$$
$$\}$$
$$w = (phi - 0.75)/(1.15 - 0.75)$$
$$Chl_{Blend} = w * Chl_{2Band} + abs(w-1) * Chl_{OCx} \tag{A.8}$$

NDCI (Mishra and Mishra, 2012):

$$Chl_{NDCI} = a + b \times \left(\frac{R_{rs}(708) - R_{rs}(665)}{R_{rs}(708) + R_{rs}(665)}\right) + c \times \left(\frac{R_{rs}(708) - R_{rs}(665)}{R_{rs}(708) + R_{rs}(665)}\right)^2$$
$$A = 14.039,\ b = 86.11,\ c = 194.325 \tag{A.9}$$

Table A.1
Stratified performance metrics for the three algorithms implemented for MSI-simulated R_{rs}. The MDN model exhibits major improvements over OC3 and Blend in mesotrophic and eutrophic waters, although the improved performance is not as significant in hypereutrophic waters.

	MSI	RMSE	Slope	MAPE	RMSLE	Bias	MAE	MWR
TSI ≤30 Chl*a* ≤ 0.94 (n=186) Median = 0.5 (mg/m^3)	MDN	2.890	0.815	26.7	0.753	1.137	1.319	NA
	OC4	12.770	1.208	125.0	1.412	2.250	2.250	86.9
	Blend	79.320	0.635	201.4	1.971	3.014	3.037	90.7
30 < TSI ≤ 40 0.94 < Chl*a* ≤ 2.6 (n=290) Median = 1.7 (mg/m^3)	MDN	5.696	1.105	334.4	0.797	1.163	1.432	NA
	OC4	17.635	0.991	219.7	1.713	3.197	3.450	89.9
	Blend	18.403	1.006	289.6	1.782	3.896	4.003	93.3
40 < TSI ≤ 50 2.6 <Chl*a* ≤ 6.4 (n=352) Median = 4.2 (mg/m^3)	MDN	17.787	0.896	24.9	0.627	1.023	1.274	NA
	OC4	18.172	0.474	113.1	1.205	2.131	2.172	83.2
	Blend	23.031	0.380	141.5	1.216	2.415	2.428	88.7
50 < TSI ≤ 60 6.4 <Chl*a* ≤ 20 (n=568) Median = 11.8 (mg/m^3)	MDN	7.427	0.903	21.5	0.434	0.993	1.250	NA
	OC4	16.238	0.118	48.4	0.782	1.087	1.669	72.9
	Blend	12.276	0.449	41.1	0.623	1.336	1.461	66.9
60 < TSI ≤ 70 20 <Chl*a* ≤ 56 (n=357) Median = 28.4 (mg/m^3)	MDN	36.379	1.047	17.6	0.436	0.909	1.205	NA
	OC4	39.712	0.632	50.1	0.995	0.608	1.862	79.8
	Blend	17.481	0.947	23.8	0.403	1.029	1.261	59.6
70 < TSI ≤ 80 56 < Chl*a* ≤ 154 (n=161) Median = 86.1 (mg/m^3)	MDN	37.246	0.885	17.7	0.751	0.844	1.214	NA
	OC4	80.631	0.481	82.6	1.779	0.204	4.892	88.8
	Blend	41.989	0.723	35.2	0.689	0.651	1.536	63.8
TSI > 80 Chl*a* > 154 (n=29) Median = 195.3 (mg/m^3)	MDN	196.018	0.610	47.8	1.043	0.521	1.918	NA
	OC4	271.358	0.801	93.7	2.677	0.062	16.03	96.2
	Blend	214.340	0.704	53.6	1.402	0.464	2.157	80.8

Table A.2
The overall performance analyses of various algorithms tested for MSI and OLCI simulated *in situ* R_{rs}. The MDN model provides enhanced predictions for Chl*a* for both missions with OLCI giving out slightly smaller errors.

	RMSE (mg/m^3)	Slope	MAPE (%)	RMSLE	Bias	MAE	MWR (%)	Negative estimates
				MSI (n = 1943)				
MDN	30.31	0.876	24.0	0.616	0.995	1.275	N/A	0
OC2	17,103.2	0.463	67.2	1.356	1.092	2.116	79.1	0
OC3	43.25	0.484	74.5	1.276	1.419	2.137	81.7	0
OCx	43.19	0.496	74.6	1.499	1.409	2.145	81.7	0
2-Band	40.12	0.530	63.9	1.252	1.448	1.687	74.4	111
3-Band	72.692	0.428	88.0	1.415	1.669	1.841	78.4	159
Blend	40.77	0.585	62.1	1.199	1.550	1.757	76.5	0
NDCI	33.39	0.329	48.9	1.263	1.104	1.714	72.6	0
				OLCI (n = 1905)				
MDN	26.98	0.865	22.9	0.581	1.003	1.265	N/A	0
OC4	3364.6	0.581	81.0	1.309	1.645	2.221	82.7	0
OCx	47.33	0.581	83.3	1.495	1.678	2.247	83.7	0
2-Band	28.37	0.590	50.9	1.188	1.129	1.502	71.4	241
3-Band	42.80	0.475	66.2	1.207	1.291	1.529	73.1	310
Blend	31.66	0.624	69.3	1.351	1.640	1.867	77.1	0
NDCI	31.10	0.297	50.6	1.302	0.969	1.843	78.8	0

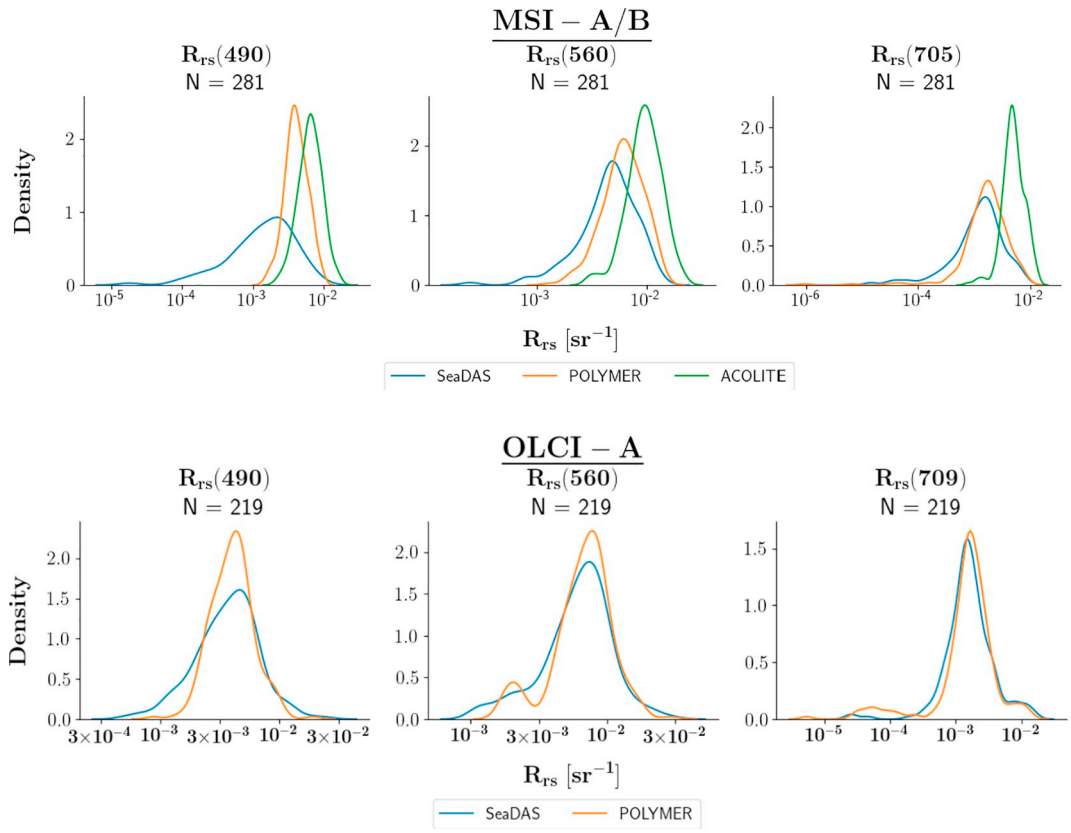

Fig. A.1. Normalized frequency distributions of MSI- and OLCI-derived R_{rs} for the common matchups processed via the corresponding processors.

References

Agarap, A.F., 2018. Deep Learning using Rectified Linear Units (ReLU). arXiv preprint. arXiv:1803.08375.

Ansper, A., Alikas, K., 2019. Retrieval of chlorophyll a from Sentinel-2 MSI data for the European Union water framework directive reporting purposes. Remote Sens. 11, 64.

Binding, C.E., Greenberg, T.A., Bukata, R.P., 2011. Time series analysis of algal blooms in Lake of the Woods using the MERIS maximum chlorophyll index. J. Plankton Res. 33, 1847–1852.

Bishop, C.M., 1994. Mixture density networks. In: NCRG/94/004. Aston University, Birmingham. http://www.ncrg.aston.ac.uk.

Brooks, B.W., Lazorchak, J.M., Howard, M.D., Johnson, M.V.V., Morton, S.L., Perkins, D.A., Reavie, E.D., Scott, G.I., Smith, S.A., Steevens, J.A., 2016. Are harmful algal blooms becoming the greatest inland water quality threat to public health and aquatic ecosystems? Environ. Toxicol. Chem. 35, 6–13.

Bukata, R., Jerome, J., Bruton, J., Jain, S., Zwick, H., 1981. Optical water quality model of Lake Ontario. 1: determination of the optical cross sections of organic and inorganic particulates in Lake Ontario. Appl. Opt. 20, 1696–1703.

Bulgarelli, B., Kiselev, V., Zibordi, G., 2014. Simulation and analysis of adjacency effects in coastal waters: a case study. Appl. Opt. 53, 1523–1545.

Buschmann, C., Langsdorf, G., Lichtenthaler, H., 2000. Imaging of the blue, green, and red fluorescence emission of plants: an overview. Photosynthetica 38, 483–491.

Carlson, R.E., 1977. A trophic state index for lakes 1. Limnol. Oceanogr. 22, 361–369.

Carmichael, W.W., 2001. Health effects of toxin-producing cyanobacteria:"the CyanoHABs" Hum. Ecol. Risk Assess. Int. J. 7, 1393–1407.

Carvalho, L., McDonald, C., de Hoyos, C., Mischke, U., Phillips, G., Borics, G., Poikane, S., Skjelbred, B., Solheim, A.L., Van Wichelen, J., 2013. Sustaining recreational quality of European lakes: minimizing the health risks from algal blooms through phosphorus control. J. Appl. Ecol. 50, 315–323.

Cazzaniga, I., Bresciani, M., Colombo, R., Della Bella, V., Padula, R., Giardino, C., 2019. A comparison of Sentinel-3-OLCI and Sentinel-2-MSI-derived chlorophyll-a maps for two large Italian lakes. Remote Sens. Lett. 10, 978–987.

Defoin-Platel, M., Chami, M., 2007. How ambiguous is the inverse problem of ocean color in coastal waters? J. Geophys. Res. Oceans 112.

Dekker, A., Malthus, T., Wijnen, M., Seyhan, E., 1992. Remote sensing as a tool for assessing water quality in Loosdrecht lakes. Hydrobiologia 233, 137–159.

Doerffer, R., Schiller, H., 2007. The MERIS case 2 water algorithm. Int. J. Remote Sens. 28, 517–535.

Donlon, C., Berruti, B., Buongiorno, A., Ferreira, M.-H., Féménias, P., Frerick, J., Goryl, P., Klein, U., Laur, H., Mavrocordatos, C., 2012. The global monitoring for environment and security (GMES) sentinel-3 mission. Remote Sens. Environ. 120, 37–57.

Dörnhöfer, K., Klinger, P., Heege, T., Oppelt, N., 2018. Multi-sensor satellite and in situ monitoring of phytoplankton development in a eutrophic-mesotrophic lake. Sci. Total Environ. 612, 1200–1214.

Doxani, G., Vermote, E., Roger, J.-C., Gascon, F., Adriaensen, S., Frantz, D., Hagolle, O., Hollstein, A., Kirches, G., Li, F., 2018. Atmospheric correction inter-comparison exercise. Remote Sens. 10, 352.

Drusch, M., Del Bello, U., Carlier, S., Colin, O., Fernandez, V., Gascon, F., Hoersch, B., Isola, C., Laberinti, P., Martimort, P., 2012. Sentinel-2: ESA's optical high-resolution mission for GMES operational services. Remote Sens. Environ. 120, 25–36.

Duan, H., Ma, R., Xu, X., Kong, F., Zhang, S., Kong, W., Hao, J., Shang, L., 2009. Two-decade reconstruction of algal blooms in China's Lake Taihu. Environ. Sci. Technol. 43, 3522–3528.

ESA, & EUMETSAT, 2019. Sentinel-3 product notice – OLCI Level-2 ocean colour. EUMETSAT. E.M. Management. 1.

Freitas, F.H., Dierssen, H.M., 2019. Evaluating the seasonal and decadal performance of red band difference algorithms for chlorophyll in an optically complex estuary with winter and summer blooms. Remote Sens. Environ. 231, 111228.

Frouin, R., Deschamps, P.-Y., Ramon, D., Steinmetz, F., 2012. Improved Ocean-Color Remote Sensing in the Arctic Using the POLYMER Algorithm. (pp. 85250I-85250I-85212).

Gernez, P., Doxaran, D., Barillé, L., 2017. Shellfish aquaculture from space: potential of Sentinel2 to monitor tide-driven changes in turbidity, chlorophyll concentration and oyster physiological response at the scale of an oyster farm. Front. Mar. Sci. 4, 137.

Giardino, C., Brando, V.E., Dekker, A.G., Strombeck, N., Candiani, G., 2007. Assessment of water quality in Lake Garda (Italy) using Hyperion. Remote Sens. Environ. 109, 183–195.

Gilerson, A.A., Gitelson, A.A., Zhou, J., Gurlin, D., Moses, W., Ioannou, I., Ahmed, S.A., 2010. Algorithms for remote estimation of chlorophyll-a in coastal and inland waters using red and near infrared bands. Opt. Express 18, 24109–24125.

Gitelson, A., 1992. The peak near 700 nm on radiance spectra of algae and water: relationships of its magnitude and position with chlorophyll concentration. Int. J. Remote Sens. 13, 3367–3373.

Gitelson, A.A., Schalles, J.F., Hladik, C.M., 2007. Remote chlorophyll-a retrieval in turbid, productive estuaries: Chesapeake Bay case study. Remote Sens. Environ. 109, 464–472.

Gitelson, A.A., Gurlin, D., Moses, W.J., Barrow, T., 2009. A bio-optical algorithm for the remote estimation of the chlorophyll-a concentration in case 2 waters. Environ. Res. Lett. 4, 045003.

Gons, H.J., 1999. Optical teledetection of chlorophyll a in turbid inland waters. Environ. Sci. Technol. 33, 1127–1132.

Gons, H.J., Auer, M.T., Effler, S.W., 2008. MERIS satellite chlorophyll mapping of oligotrophic and eutrophic waters in the Laurentian Great Lakes. Remote Sens. Environ. 112, 4098–4106.

Gordon, H.R., Wang, M., 1994. Retrieval of water-leaving radiance and aerosol optical

thickness over the oceans with SeaWiFS: a preliminary algorithm. Appl. Opt. 33, 443–452.
Gordon, H.R., Clark, D.K., Brown, J.W., Brown, O.B., Evans, R.H., Broenkow, W.W., 1983. Phytoplankton pigment concentrations in the Middle Atlantic Bight: comparison of ship determinations and CZCS estimates. Appl. Opt. 22, 20–36.
Gower, J., Borstad, G., 1990. Mapping of phytoplankton by solar-stimulated fluorescence using an imaging spectrometer. Int. J. Remote Sens. 11, 313–320.
Gower, J., King, S., 2012. Use of satellite images of chlorophyll fluorescence to monitor the spring bloom in coastal waters. Int. J. Remote Sens. 33, 7469–7481.
Gower, J., King, S., Borstad, G., Brown, L., 2005. Detection of intense plankton blooms using the 709 nm band of the MERIS imaging spectrometer. Int. J. Remote Sens. 26, 2005–2012.
Gurlin, D., Gitelson, A.A., Moses, W.J., 2011. Remote estimation of chl-a concentration in turbid productive waters—return to a simple two-band NIR-red model? Remote Sens. Environ. 115, 3479–3490.
Holben, B.N., Eck, T.F., Slutsker, I., Tanré, D., Buis, J.P., Setzer, A., Vermote, E., Reagan, J.A., Kaufman, Y.J., Nakajima, T., Lavenu, F., Jankowiak, I., Smirnov, A., 1998. AERONET—A federated instrument network and data archive for aerosol characterization. Remote Sens. Environ. 66, 1–16.
Holm-Hansen, O., Riemann, B., 1978. Chlorophyll a determination: improvements in methodology. Oikos 438–447.
Hu, C., Lee, Z., Franz, B., 2012. Chlorophylla algorithms for oligotrophic oceans: a novel approach based on three-band reflectance difference. J. Geophys. Res. Oceans 117.
Ibrahim, A., Franz, B.A., Ahmad, Z., Bailey, S.W., 2019. Multi-band atmospheric correction algorithm for ocean color retrievals. Front. Earth Sci. 7, 116.
Jain, S., Miller, J., 1976. Subsurface water parameters: optimization approach to their determination from remotely sensed water color data. Appl. Opt. 15, 886–890.
Jeffrey, S.t., Humphrey, G., 1975. New spectrophotometric equations for determining chlorophylls a, b, c1 and c2 in higher plants, algae and natural phytoplankton. Biochem. Physiol. Pflanz. 167, 191–194.
Le, C., Hu, C., Cannizzaro, J., English, D., Muller-Karger, F., Lee, Z., 2013. Evaluation of chlorophyll-a remote sensing algorithms for an optically complex estuary. Remote Sens. Environ. 129, 75–89.
Lee, Z., Carder, K.L., Arnone, R.A., 2002. Deriving inherent optical properties from water color: a multiband quasi-analytical algorithm for optically deep waters. Appl. Opt. 41, 5755–5772.
Lee, Z., Pahlevan, N., Ahn, Y.-H., Greb, S., O'Donnell, D., 2013. Robust approach to directly measuring water-leaving radiance in the field. Appl. Opt. 52, 1693–1701.
Letelier, R.M., Abbott, M.R., 1996. An analysis of chlorophyll fluorescence algorithms for the moderate resolution imaging spectrometer (MODIS). Remote Sens. Environ. 58, 215–223.
Marshall, H., 1994. Chesapeake bay phytoplankton. 1. Composition. Proc. Biol. Soc. Wash. 107, 573–585.
Marshall, H.G., 1996. Toxin producing phytoplankton in Chesapeake Bay. Virginia Journal of Science 47.
Marshall, H.G., Lacouture, R.V., Buchanan, C., Johnson, J.M., 2006. Phytoplankton assemblages associated with water quality and salinity regions in Chesapeake Bay, USA. Estuar. Coast. Shelf Sci. 69, 10–18.
Matsushita, B., Yang, W., Yu, G., Oyama, Y., Yoshimura, K., Fukushima, T., 2015. A hybrid algorithm for estimating the chlorophyll-a concentration across different trophic states in Asian inland waters. ISPRS J. Photogramm. Remote Sens. 102, 28–37.
Matthews, M.W., Odermatt, D., 2015. Improved algorithm for routine monitoring of cyanobacteria and eutrophication in inland and near-coastal waters. Remote Sens. Environ. 156, 374–382.
Matthews, M.W., Bernard, S., Robertson, L., 2012. An algorithm for detecting trophic status (chlorophyll-a), cyanobacterial-dominance, surface scums and floating vegetation in inland and coastal waters. Remote Sens. Environ. 124, 637–652.
McKee, D., Cunningham, A., Dudek, A., 2007. Optical water type discrimination and tuning remote sensing band-ratio algorithms: application to retrieval of chlorophyll and Kd (490) in the Irish and Celtic seas. Estuar. Coast. Shelf Sci. 73, 827–834.
Mei, L., Rozanov, V., Vountas, M., Burrows, J.P., Levy, R.C., Lotz, W., 2017. Retrieval of aerosol optical properties using MERIS observations: algorithm and some first results. Remote Sens. Environ. 197, 125–140.
Mélin, F., Vantrepotte, V., Chuprin, A., Grant, M., Jackson, T., Sathyendranath, S., 2017. Assessing the fitness-for-purpose of satellite multi-mission ocean color climate data records: a protocol applied to OC-CCI chlorophyll-a data. Remote Sens. Environ. 203, 139–151.
Metcalf, J.S., Banack, S.A., Powell, J.T., Tymm, F.J., Murch, S.J., Brand, L.E., Cox, P.A., 2018. Public health responses to toxic cyanobacterial blooms: perspectives from the 2016 Florida event. Water Policy 20, 919–932.
Mishra, S., Mishra, D.R., 2012. Normalized difference chlorophyll index: a novel model for remote estimation of chlorophyll-a concentration in turbid productive waters. Remote Sens. Environ. 117, 394–406.
Mittenzwey, K.H., Ullrich, S., Gitelson, A., Kondratiev, K., 1992. Determination of chlorophyll a of inland waters on the basis of spectral reflectance. Limnol. Oceanogr. 37, 147–149.
Mobley, C.D., 1994. Light and Water: Radiative Transfer in Natural Waters. Academic Press, Inc.
Mograne, M.A., Jamet, C., Loisel, H., Vantrepotte, V., Mériaux, X., Cauvin, A., 2019. Evaluation of five atmospheric correction algorithms over French optically-complex waters for the sentinel-3A OLCI Ocean color sensor. Remote Sens. 11, 668.
Moore, T.S., Campbell, J.W., Feng, H., 2001. A fuzzy logic classification scheme for selecting and blending satellite ocean color algorithms. IEEE Trans. Geosci. Remote Sens. 39, 1764–1776.
Moses, W.J., Gitelson, A.A., Berdnikov, S., Povazhnyy, V., 2009a. Estimation of chlorophyll-a concentration in case II waters using MODIS and MERIS data—-successes and challenges. Environ. Res. Lett. 4, 045005.
Moses, W.J., Gitelson, A.A., Berdnikov, S., Povazhnyy, V., 2009b. Satellite estimation of chlorophyll-a concentration using the red and NIR bands of MERISThe Azov Sea case study. IEEE Geosci. Remote Sens. Lett. 6, 845–849.
Moses, W.J., Gitelson, A.A., Berdnikov, S., Saprygin, V., Povazhnyi, V., 2012. Operational MERIS-based NIR-red algorithms for estimating chlorophyll-a concentrations in coastal waters—the Azov Sea case study. Remote Sens. Environ. 121, 118–124.
Mouw, C.B., Greb, S., Aurin, D., DiGiacomo, P.M., Lee, Z., Twardowski, M., Binding, C., Hu, C., Ma, R., Moore, T., 2015. Aquatic color radiometry remote sensing of coastal and inland waters: challenges and recommendations for future satellite missions. Remote Sens. Environ. 160, 15–30.
Mueller, J.L., Morel, A., Frouin, R., Davis, C., Arnone, R., Carder, K., Lee, Z., Steward, R., Hooker, S., Mobley, C., 2003. Ocean Optics Protocols for Satellite Ocean Color Sensor Validation, Revision 4. Volume III: Radiometric Measurements and Data Analysis Protocols.
Neil, C., Spyrakos, E., Hunter, P.D., Tyler, A.N., 2019. A global approach for chlorophyll-a retrieval across optically complex inland waters based on optical water types. Remote Sens. Environ. 229, 159–178.
Novoa, S., Chust, G., Sagarminaga, Y., Revilla, M., Borja, A., Franco, J., 2012. Water quality assessment using satellite-derived chlorophyll-a within the European directives, in the southeastern Bay of Biscay. Mar. Pollut. Bull. 64, 739–750.
Odermatt, D., Danne, O., Philipson, P., Brockmann, C., 2018. Diversity II water quality parameters from ENVISAT (2002－2012): a new global information source for lakes. Earth Syst. Sci. Data 10.
O'Reilly, J.E., Werdell, P.J., 2019. Chlorophyll algorithms for ocean color sensors-OC4, OC5 & OC6. Remote Sens. Environ. 229, 32–47.
O'Reilly, J.E., Maritorena, S., Mitchell, B.G., Siegel, D.A., Carder, K.L., Garver, S.A., Kahru, M., McClain, C., 1998. Ocean color chlorophyll algorithms for SeaWiFS. J. Geophys. Res. Oceans 103, 24937–24953.
Pahlevan, N., Sarkar, S., Franz, B.A., 2016. Uncertainties in coastal ocean color products: impacts of spatial sampling. Remote Sens. Environ. 181, 14–26.
Pahlevan, N., Roger, J.-C., Ahmad, Z., 2017a. Revisiting short-wave-infrared (SWIR) bands for atmospheric correction in coastal waters. Opt. Express 25, 6015–6035.
Pahlevan, N., Sarkar, S., Franz, B.A., Balasubramanian, S.V., He, J., 2017b. Sentinel-2 MultiSpectral instrument (MSI) data processing for aquatic science applications: demonstrations and validations. Remote Sens. Environ. 201, 47–56.
Pahlevan, N., Schott, J.R., Franz, B.A., Zibordi, G., Markham, B., Bailey, S., Schaaf, C.B., Ondrusek, M., Greb, S., Strait, C.M., 2017c. Landsat 8 remote sensing reflectance (R rs) products: evaluations, intercomparisons, and enhancements. Remote Sens. Environ. 190, 289–301.
Pahlevan, N., Chittimalli, S.K., Balasubramanian, S.V., Vellucci, V., 2019. Sentinel-2/Landsat-8 product consistency and implications for monitoring aquatic systems. Remote Sens. Environ. 220, 19–29.
Palmer, S.C., Hunter, P.D., Lankester, T., Hubbard, S., Spyrakos, E., Tyler, A.N., Presing, M., Horvath, H., Lamb, A., Balzter, H., 2015. Validation of Envisat MERIS algorithms for chlorophyll retrieval in a large, turbid and optically-complex shallow lake. Remote Sens. Environ. 157, 158–169.
Preusker, R., Lindstrot, R., 2009. Remote sensing of cloud-top pressure using moderately resolved measurements within the oxygen A band—a sensitivity study. J. Appl. Meteorol. Climatol. 48, 1562–1574.
Roesler, C., Uitz, J., Claustre, H., Boss, E., Xing, X., Organelli, E., Briggs, N., Bricaud, A., Schmechtig, C., Poteau, A., 2017. Recommendations for obtaining unbiased chlorophyll estimates from in situ chlorophyll fluorometers: a global analysis of WET labs ECO sensors. Limnol. Oceanogr. Methods 15, 572–585.
Ruddick, K.G., Voss, K., Boss, E., Castagna, A., Frouin, R., Gilerson, A., Hieronymi, M., Johnson, B.C., Kuusk, J., Lee, Z., 2019. A review of protocols for fiducial reference measurements of water-leaving radiance for validation of satellite remote-sensing data over water. Remote Sens. 11, 2198.
Santer, R., Schmechtig, C., 2000. Adjacency effects on water surfaces: primary scattering approximation and sensitivity study. Appl. Opt. 39, 361–375.
Schalles, J.F., 2006. Optical remote sensing techniques to estimate phytoplankton chlorophyll a concentrations in coastal. In: Remote Sensing of Aquatic Coastal Ecosystem Processes. Springer, pp. 27–79.
Schmidt, G., 2011. Relational Mathematics. Cambridge University Press.
Schroeder, T., Schaale, M., Fischer, J., 2007. Retrieval of atmospheric and oceanic properties from MERIS measurements: a new case-2 water processor for BEAM. Int. J. Remote Sens. 28, 5627–5632.
Seegers, B.N., Stumpf, R.P., Schaeffer, B.A., Loftin, K.A., Werdell, P.J., 2018. Performance metrics for the assessment of satellite data products: an ocean color case study. Opt. Express 26, 7404–7422.
Shuchman, R.A., Leshkevich, G., Sayers, M.J., Johengen, T.H., Brooks, C.N., Pozdnyakov, D., 2013. An algorithm to retrieve chlorophyll, dissolved organic carbon, and suspended minerals from Great Lakes satellite data. J. Great Lakes Res. 39, 14–33.
Smith, R., Baker, K., 1982. Oceanic chlorophyll concentrations as determined by satellite (Nimbus-7 coastal zone color scanner). Mar. Biol. 66, 269–279.
Smith, M.E., Lain, L.R., Bernard, S., 2018. An optimized chlorophyll a switching algorithm for MERIS and OLCI in phytoplankton-dominated waters. Remote Sens. Environ. 215 (217–227).
Spyrakos, E., O'Donnell, R., Hunter, P.D., Miller, C., Scott, M., Simis, S.G., Neil, C., Barbosa, C.C., Binding, C.E., Bradt, S., 2018. Optical types of inland and coastal waters. Limnol. Oceanogr. 63, 846–870.
Steinmetz, F., Deschamps, P.-Y., Ramon, D., 2011. Atmospheric correction in presence of sun glint: application to MERIS. Opt. Express 19, 9783–9800.
Stumpf, R.P., Tyler, M.A., 1988. Satellite detection of bloom and pigment distributions in estuaries. Remote Sens. Environ. 24, 385–404.

Sydor, M., Gould, R.W., Arnone, R.A., Haltrin, V.I., Goode, W., 2004. Uniqueness in remote sensing of the inherent optical properties of ocean water. Appl. Opt. 43, 2156–2162.
Tang, D., Kawamura, H., Lee, M.-A., Van Dien, T., 2003. Seasonal and spatial distribution of chlorophyll-a concentrations and water conditions in the Gulf of Tonkin, South China Sea. Remote Sens. Environ. 85, 475–483.
Toming, K., Kutser, T., Laas, A., Sepp, M., Paavel, B., Nõges, T., 2016. First experiences in mapping lake water quality parameters with Sentinel-2 MSI imagery. Remote Sens. 8, 640.
Tzortziou, M., Subramaniam, A., Herman, J.R., Gallegos, C.L., Neale, P.J., Harding, J.L.W., 2007. Remote sensing reflectance and inherent optical properties in the mid Chesapeake Bay. Estuar. Coast. Shelf Sci. 72, 16–32.
Vanhellemont, Q., 2019. Adaptation of the dark spectrum fitting atmospheric correction for aquatic applications of the Landsat and Sentinel-2 archives. Remote Sens. Environ. 225, 175–192.
Vanhellemont, Q., Ruddick, K., 2014. Turbid wakes associated with offshore wind turbines observed with Landsat 8. Remote Sens. Environ. 145, 105–115.
Vermote, E., Justice, C., Claverie, M., Franch, B., 2016. Preliminary analysis of the performance of the Landsat 8/OLI land surface reflectance product. Remote Sens. Environ. 185, 46–56.
Vertucci, F.A., Likens, G.E., 1989. Spectral reflectance and water quality of Adirondack mountain region lakes. Limnol. Oceanogr. 34, 1656–1672.
Vilas, L.G., Spyrakos, E., Palenzuela, J.M.T., 2011. Neural network estimation of chlorophyll a from MERIS full resolution data for the coastal waters of Galician rias (NW Spain). Remote Sens. Environ. 115, 524–535.
Warren, M.A., Simis, S.G., Martinez-Vicente, V., Poser, K., Bresciani, M., Alikas, K., Spyrakos, E., Giardino, C., Ansper, A., 2019. Assessment of atmospheric correction algorithms for the sentinel-2A MultiSpectral imager over coastal and inland waters. Remote Sens. Environ. 225, 267–289.
Welschmeyer, N.A., 1994. Fluorometric analysis of chlorophyll a in the presence of chlorophyll b and pheopigments. Limnol. Oceanogr. 39, 1985–1992.
Werdell, P.J., Bailey, S.W., 2005. An improved in-situ bio-optical data set for ocean color algorithm development and satellite data product validation. Remote Sens. Environ. 98, 122–140.
Williams, C.D., Burns, J., Chapman, A., Flewelling, L., Pawlowicz, M., Carmichael, W., 2001. Assessment of Cyanotoxins in Florida's Lakes, Reservoirs, and Rivers. (St. Johns River Water Management District).
Wynne, T.T., Stumpf, R.P., Tomlinson, M.C., Dyble, J., 2010. Characterizing a cyanobacterial bloom in western Lake Erie using satellite imagery and meteorological data. Limnol. Oceanogr. 55, 2025–2036.
Yacobi, Y.Z., Gitelson, A., Mayo, M., 1995. Remote sensing of chlorophyll in Lake Kinneret using highspectral-resolution radiometer and Landsat TM: spectral features of reflectance and algorithm development. J. Plankton Res. 17, 2155–2173.
Yang, W., Matsushita, B., Chen, J., Fukushima, T., 2011. Estimating constituent concentrations in case II waters from MERIS satellite data by semi-analytical model optimizing and look-up tables. Remote Sens. Environ. 115, 1247–1259.
Yoder, J.A., McClain, C.R., Feldman, G.C., Esaias, W.E., 1993. Annual cycles of phytoplankton chlorophyll concentrations in the global ocean: a satellite view. Glob. Biogeochem. Cycles 7, 181–193.
Zhang, M., Hu, C., Cannizzaro, J., English, D., Barnes, B.B., Carlson, P., Yarbro, L., 2018. Comparison of two atmospheric correction approaches applied to MODIS measurements over north American waters. Remote Sens. Environ. 216, 442–455.